JGR Oceans

RESEARCH ARTICLE
10.1029/2021JC018178

Dissipation and Bathymetric Sensitivities in an Unstructured Mesh Global Tidal Model

Coleman P. Blakely[1], Guoming Ling[1], William J. Pringle[2], María Teresa Contreras[1], Damrongsak Wirasaet[1], Joannes J. Westerink[1], Saeed Moghimi[3,4], Greg Seroka[3], Lei Shi[3], Edward Myers[3], Margaret Owensby[5], and Chris Massey[5]

[1]Department of Civil and Environmental Engineering and Earth Sciences, University of Notre Dame, Notre Dame, IN, USA, [2]Environmental Science Division, Argonne National Laboratory, Lemont, IL, USA, [3]NOAA National Ocean Service, Office of Coast Survey, National Oceanic and Atmospheric Administration, Silver Spring, MD, USA, [4]University Corporation for Atmospheric Research, Boulder, CO, USA, [5]Coastal and Hydraulics Laboratory, Engineer Research and Development Center, U.S. Army Corps of Engineers, Vicksburg, MS, USA

Abstract The mechanisms and geographic distribution of global tidal dissipation in barotropic tidal models are examined using a high resolution unstructured mesh finite element model. Mesh resolution varies between 2 and 25 km and is especially focused on inner shelves and steep bathymetric gradients. Tidal response sensitivities to bathymetric changes are examined to put into context response sensitivities to frictional processes. We confirm that the Ronne Ice Shelf dramatically affects Atlantic tides but also find that bathymetry in the Hudson Bay system is a critical control. We follow a sequential frictional parameter optimization process and use TPXO9 data-assimilated tidal elevations as a reference solution. From simulated velocities and depths, dissipation within the global model is estimated and allows us to pinpoint dissipation at high resolution. Boundary layer dissipation is extremely focused with 1.4% of the ocean accounting for 90% of the total. Internal tide friction is much more distributed with 16.7% of the ocean accounting for 90% of the total. Often highly regional dissipation can impact basin-scale and even ocean wide tides. Optimized boundary layer friction parameters correlate very well with the physical characteristics of the locality with high friction factors associated with energetic tidal regions, deep ocean island chains, and ice covered areas. Global complex M_2 tide errors are 1.94 cm in deep waters. Total global boundary layer and internal tide dissipation are estimated, respectively, at 1.83 and 1.49 TW. This continues the trend in the literature toward attributing more dissipation to internal tides.

Plain Language Summary This study studies how and where tides dissipate energy in the ocean. Using current speeds and water levels, it is possible to estimate how much energy the ocean dissipates and find areas that are particularly energetic. An important aspect of tidal modeling is accurately setting the depth of the ocean. We identify areas of the ocean where it is very important to have accurate water depths for accurate results by using different bathymetric databases. Additionally, we find what areas of the ocean are sensitive to changes in energy dissipation. This is done via altering frictional coefficients in our model for both friction between the ocean floor and the bottom of the water column, and for internal waves that are generated near steep topography with strong vertical density gradients. With this information, we determine optimal friction coefficients, improving the tides in our model. We find that the friction coefficients obtained through the optimization process correlate well to the physical characteristics of the assigned regions. We also determine where and how energy is dissipated enabling us to pinpoint the most significant dissipation regions.

Key Points:

- Boundary layer dissipation is concentrated in a small portion of the ocean while baroclinic conversion is more distributed
- Boundary layer dissipation on certain shelves controls basin-scale tides
- Frictional coefficients derived via optimization methods are consistent with regional physical and hydrodynamic characteristics

Correspondence to:
C. P. Blakely,
cblakely@nd.edu

Citation:
Blakely, C. P., Ling, G., Pringle, W. J., Contreras, M. T., Wirasaet, D., Westerink, J. J., et al. (2022). Dissipation and bathymetric sensitivities in an unstructured mesh global tidal model. *Journal of Geophysical Research: Oceans*, *127*, e2021JC018178. https://doi.org/10.1029/2021JC018178

Received 3 NOV 2021
Accepted 4 MAY 2022

Author Contributions:
Conceptualization: Coleman P. Blakely, William J. Pringle, María Teresa Contreras, Damrongsak Wirasaet, Joannes J. Westerink, Lei Shi
Formal analysis: Coleman P. Blakely
Funding acquisition: William J. Pringle, Joannes J. Westerink
Investigation: Coleman P. Blakely, Guoming Ling, Joannes J. Westerink
Methodology: Coleman P. Blakely, William J. Pringle, Damrongsak Wirasaet, Joannes J. Westerink, Lei Shi
Project Administration: Joannes J. Westerink, Saeed Moghimi, Edward Myers, Chris Massey
Resources: Margaret Owensby, Chris Massey
Software: William J. Pringle, Damrongsak Wirasaet

1. Introduction

The primary dissipation mechanisms for global tides are boundary layer dissipation and internal tide dissipation from barotropic to baroclinic tidal conversion (Munk, 1997). From early estimates of total tidal dissipation characterized solely by boundary layer dissipation by Taylor and Shaw (1920) and Jeffreys (1921) to sophisticated estimates using altimeter data and assimilated tidal models performed by Egbert and Ray (2001) and Green and Nycander (2013), our understanding of where the astronomical energy imparted on the oceans is dissipated has grown tremendously. While there is some uncertainty in where tidal dissipation predominantly occurs in nature, it is relatively well accepted that tides dissipate approximately 3.5 TW of energy (Munk, 1997). What is more unclear is the distribution between internal tide dissipation and boundary layer dissipation. Munk (1997) estimates 2.6 TW of dissipation on the shelves and 0.9 TW dissipated through internal tides. Egbert and Ray (2001)

Supervision: Joannes J. Westerink, Saeed Moghimi, Greg Seroka, Edward Myers, Margaret Owensby, Chris Massey
Validation: Coleman P. Blakely, Guoming Ling
Visualization: Coleman P. Blakely
Writing – original draft: Coleman P. Blakely
Writing – review & editing: Coleman P. Blakely, Guoming Ling, William J. Pringle, María Teresa Contreras, Damrongsak Wirasaet, Joannes J. Westerink, Saeed Moghimi, Greg Seroka, Lei Shi, Margaret Owensby, Chris Massey

estimate that 1 TW or more could be dissipated in the deep ocean (where dissipation is dominated by internal tides). Furthermore Green and Nycander (2013) raise their estimate of internal tide dissipation to 1.18 TW.

This study applies a high resolution unstructured mesh to more closely examine the effects of bathymetry and frictional parameterizations on global tides. Our mesh resolution ranges from 2 km nearshore and across steep topographic gradients to 25 km in deep waters with mild slopes. We use the OceanMesh2D mesh generation toolbox and the Advanced Circulation Ocean Model (ADCIRC). The former allows for the creation of high quality, global to channel scale, unstructured triangulated meshes driven by geometric and hydrodynamic characterization parameters (Roberts et al., 2019). The latter is a finite element method shallow water equation (SWE) solver used for modeling of regional, coastal, and global ocean systems (Pringle et al., 2021; Westerink et al., 2008).

It is important to put into context the magnitude of sensitivities to frictional changes by exploring how changes in bathymetry within our model can affect tides. Past studies have shown that certain regions are highly sensitive to bathymetric perturbations (Jeon et al., 2019; Sulzbach et al., 2021; X. Wang, Verlaan, et al., 2021; Wilmes & Green, 2014). This would suggest that improving bathymetry in specific locations will have significant impacts on global tides. With the continued improvement and availability of global bathymetric data sets, such as the GEBCO Bathymetric Group-gridded bathymetry and numerous high-fidelity local/regional bathymetric data sets, it is vital to assess how these different data sources can impact tides. We will show that bathymetric improvements in specific areas can have disproportionate impacts on global tidal results and are a vital hydrodynamic control.

Following the study of bathymetry, regions within our global model that dissipate large amounts of energy are identified. Based on this geographic distribution of dissipation density, a targeted sensitivity analysis is performed. By perturbing frictional coefficients, we identify regions that are particularly sensitive to perturbations in boundary layer and internal tide dissipation. In addition to highlighting areas where it is vital to use accurate frictional coefficients, these sensitivity tests help explain long-term changes in tides. As detailed in Haigh et al. (2020), tidal amplitudes and phases have shifted considerably over the past 3 centuries due to nonastronomical factors. Changes in the physical factors that control boundary layer and internal tide dissipation undoubtedly play a role in these observed changes. Our perturbations of bathymetry, bottom friction coefficients, and internal tide coefficients effectively mimic changes in ocean bedforms and vertical stratification. Our findings show that small changes in dissipation within specific regions can have basin-scale effects on tides.

There have been numerous studies on using frictional tuning parameters to improve tidal results. Approaches have varied from methodical searches of what parameters provide the best results (Lyard et al., 2006, 2021), using bedform information to select values for the open ocean (Pringle et al., 2018), adjoint-type methodologies for selecting optimal coefficients (Graham et al., 2017; Qian et al., 2021; D. Wang, Zhang, & Wang, 2021) and, in the case of overland flooding, using land use information to select values (Bunya et al., 2010). Our investigation suggests that through careful consideration of which areas of the globe are most sensitive to frictional perturbations, and through the use of cost function minimization, it is possible to more efficiently find optimal friction coefficients for these sensitive areas, resulting in a high fidelity global tidal model. We also find that these optimal parameters are consistent with the physical and hydrodynamic characteristics of the targeted regions.

2. Model Setup and Methods

2.1. Governing Equations

The governing equations used in this study are the nonconservative shallow water equations (SWEs). The form of these equations used by ADCIRC are written in spherical coordinates as follows (Pringle et al., 2021; Westerink et al., 1994):

$$\frac{\partial \eta}{\partial t} + \frac{1}{R\cos\phi}\left[\frac{\partial (UH)}{\partial \lambda} + \frac{\partial (VH\cos\phi)}{\partial \phi}\right] = 0, \tag{1}$$

$$\begin{aligned}\frac{\partial U}{\partial t} + \frac{g}{R\cos\phi}\frac{\partial \eta}{\partial \lambda} &= -\frac{U}{R\cos\phi}\frac{\partial U}{\partial \lambda} - \frac{V}{R}\frac{\partial U}{\partial \phi} + \frac{g}{R\cos\phi}\frac{\partial}{\partial \lambda}(\eta_{EQ} + \eta_{SAL}) \\ &\quad - (C_{\lambda\phi} - f)V - \left(\frac{C_d\sqrt{U^2+V^2}}{\rho_0 H} + C_{\lambda\lambda}\right)U + \frac{1}{RH}\left[\frac{\partial \tau_{\phi\phi}}{\partial \phi}\right. \\ &\quad \left. + \frac{1}{\cos\phi}\frac{\partial \tau_{\phi\lambda}}{\partial \lambda} + \tan\phi\,(\tau_{\lambda\lambda} - \tau_{\phi\phi})\right]\end{aligned} \tag{2}$$

$$\begin{aligned}\frac{\partial V}{\partial t}+\frac{g}{R}\frac{\partial \eta}{\partial \phi} &= -\frac{U}{R\cos\phi}\frac{\partial V}{\partial \lambda}-\frac{V}{R}\frac{\partial V}{\partial \phi}-\frac{g}{R}\frac{\partial}{\partial \phi}\left(\eta_{EQ}+\eta_{SAL}\right)\\ &\quad -\left(C_{\phi\lambda}+f\right)U-\left(\frac{C_d\sqrt{U^2+V^2}}{\rho_0 H}+C_{\phi\phi}\right)V\\ &\quad +\frac{1}{RH}\left[\frac{1}{\cos\phi}\frac{\partial \tau_{\lambda\lambda}}{\partial \lambda}+\frac{\partial \tau_{\lambda\phi}}{\partial \phi}+\tan\phi\left(\tau_{\lambda\lambda}-\tau_{\phi\phi}\right)\right]\end{aligned} \tag{3}$$

where η is the water surface elevation; R is the radius of the earth; U and V are the depth-averaged velocities in the zonal and meridional directions; $H = h + \eta$ is the total water column with h being the still water depth; $f = 2\Omega\sin\phi + \frac{\tan\phi}{R}U$ is the Coriolis parameter and advection in spherical coordinates with Ω being the angular velocity of the earth and ϕ being latitude; η_{EQ} is the equilibrium tide; η_{SAL} is the self-attraction and loading term (SAL); and C_d is the dimensionless bottom drag coefficient.

In this study, amplitudes and phases of the self-attraction and loading term (SAL) term are interpolated from FES2014, a global data-assimilated model (Lyard et al., 2006). This treatment is less consistent than performing the global integrals required to calculate self-attraction and loading at each time step but is both more computationally efficient and generally the most accurate approximation of this term (Arbic et al., 2018). Furthermore, due to the high accuracy of FES2014, the self-attraction and loading term (SAL) terms obtained in this fashion are sufficiently accurate for the purposes of this study (Stammer et al., 2014).

Additional dissipation terms are:

$$\begin{aligned}\boldsymbol{C} &= \begin{bmatrix} C_{\lambda\lambda} & C_{\lambda\phi} \\ C_{\phi\lambda} & C_{\phi\phi}\end{bmatrix} = \text{internal wave drag tensor}\\ \boldsymbol{\tau} &= \begin{bmatrix} \tau_{\lambda\lambda} & \tau_{\lambda\phi} \\ \tau_{\phi\lambda} & \tau_{\phi\phi}\end{bmatrix} = \text{lateral stress tensor}\\ &= \begin{bmatrix} 2\upsilon_t H\frac{1}{R\cos\phi}\frac{\partial U}{\partial \lambda} & \upsilon_t H\left[\frac{1}{R}\frac{\partial U}{\partial \phi}+\frac{1}{R\cos\phi}\frac{\partial V}{\partial \lambda}\right] \\ \upsilon_t H\left[\frac{1}{R}\frac{\partial U}{\partial \phi}+\frac{1}{R\cos\phi}\frac{\partial V}{\partial \lambda}\right] & 2\upsilon_t\frac{H}{R}\frac{\partial V}{\partial \phi}\end{bmatrix}\end{aligned}$$

A further explanation of the internal wave drag tensor is provided in Section 2.2.1. The lateral stress parameterization used is a symmetrical Smagorinski closure model where υ_t is the Smagorinski lateral eddy viscosity coefficient (Dresback et al., 2006; Smagorinsky, 1963).

While the physics of tides are largely barotropic, there are several baroclinic effects that can have appreciable effects on solutions. Among these, the most important is the dissipation due to baroclinic conversion discussed in Section 2.2.1. For this study, internal wave stresses are estimated by using decadally averaged salinity and temperature fields from the World Ocean Database (WOD; Boyer et al., 2013).

2.2. Calculation of Dissipation

2.2.1. Internal Tide Dissipation

The internal wave drag $\boldsymbol{C}$ in Equations 2 and 3 parameterizes internal tide dissipation due to barotropic to baroclinic conversion. This dissipation mechanism has a large impact in global models, especially in areas with steep bathymetric gradients coincident with strong vertical density gradients (Egbert & Ray, 2000). For the purposes of this study, a "local" parameterization, which assumes that internal waves are generated perpendicular to steep bathymetric slopes and are affected only by local topography and density gradients, was used (Pringle et al., 2018). In addition to the directional parameterization, a scalar parameterization similar to that employed in Zaron and Egbert (2006) that uses the magnitude of the topographic slope is examined. These parameterizations are, respectively:

$$\boldsymbol{C}_{directional} = C_{it}\frac{\sqrt{\left(N_b^2-\omega^2\right)\left(\bar{N}^2-\omega^2\right)}}{\omega}\begin{bmatrix} h_\lambda^2 & h_\lambda h_\phi \\ h_\lambda h_\phi & h_\phi^2 \end{bmatrix}, \tag{4}$$

$$\boldsymbol{C}_{scalar} = C_{it}\frac{\sqrt{\left(N_b^2-\omega^2\right)\left(\bar{N}^2-\omega^2\right)}}{\omega}\sqrt{h_\lambda^2+h_\phi^2}\begin{bmatrix} 1 & 0 \\ 0 & 1 \end{bmatrix} \tag{5}$$

where, C_{it} is a dimensionless tuneable scale factor; N_b and $\bar{N}$ are the Brunt-Väisälä frequencies calculated at the seabed and depth averaged, respectively; ω is the dominant tidal frequency (M_2 in this study); and h_λ and h_ϕ are the bathymetric slopes in the zonal and meridional directions. N_b and $\bar{N}$ are estimated from temperature and salinity fields from the World Ocean Database (WOD; Boyer et al., 2013). A cutoff depth above which internal tide dissipation is ignored was set at 150 m because boundary layer dissipation becomes the dominant dissipation mechanism in shallow regions (Pringle et al., 2018).

An important note is that h_λ and h_ϕ are calculated directly from bathymetric data sets and not from mesh nodal values. Bathymetric gradients are assigned using a cell-averaged approach that calculates the root mean square of the differences in bathymetry contained within the elements attached to a node (Roberts & Pringle, 2018).

2.2.2. Boundary Layer Dissipation

Boundary layer dissipation is parameterized by the quadratic friction law. Commonly, C_d is treated as a constant on the order of 3×10^{-3}. Previous studies have suggested that changing these values between commonly used values of 1×10^{-3} up to 1×10^{-2} have little global effect but can result in improved results regionally, especially on shelves and floodplains (Lyard et al., 2006; Pringle et al., 2018). We show that while this is generally the case, altering the bottom friction in specific regions around the globe can have significant basin-scale impacts on tidal results.

An alternative strategy for calculating a bottom friction coefficient is through the use of Manning's n coefficients with a depth-dependent relationship for C_d. Manning's equation has been widely used to parameterize frictional losses in rivers, over floodplains, and in coastal and ocean flows (Arcement & Schneider, 1989). Manning's n values are selected through characterization of sediment in a region, how much vegetation is present, and other bedform factors that could affect friction (Arcement & Schneider, 1989; Chow, 1959). Manning's n values are converted to bottom drag coefficients in the governing equations using the following relationship (Atkinson et al., 2011):

$$C_d = \frac{gn^2}{H^{1/3}} \tag{6}$$

where n is the selected Manning's n coefficient. A commonly used Manning n value for the open ocean is 0.022 $\mathrm{s\,m^{-1/3}}$ (Atkinson et al., 2011; Kerr et al., 2013). The inclusion of the extra $H^{-1/3}$ depth dependency in the calculation of the bottom drag coefficient results in higher boundary layer dissipation in shallow inner shelf regions and lower values across the outer shelf and in the deep ocean.

2.3. Finite Element Grid

For this study, a global unstructured mesh was generated using OceanMesh2D 3.3 (Roberts et al., 2019). The resolution ranges from 25 km in the deep ocean down to 2 km in coastal areas. The resulting mesh contains approximately 3.7 million nodes and 7.1 million elements. While numerous parameters determine resolution, of particular importance for this study is the topographic length scale, which ensures that steep topography is well resolved in the deep ocean (Pringle et al., 2021; Roberts et al., 2019). Note in Figure 1 the targeted resolution over mid ocean ridges, across shelf breaks, and over submerged mountain chains. By placing high resolution in such areas, the steep bathymetric gradients are more accurately resolved, allowing for a better representation of the local currents and of the parameterization of internal tide dissipation. Boundary layer dissipation is well captured because it is focused mainly in shallow inner shelf and coastal regions that also have targeted high resolution. Bathymetric data sets used to develop this mesh are described and analyzed in Section 4. For all simulations, a minimum depth of 5 m was enforced.

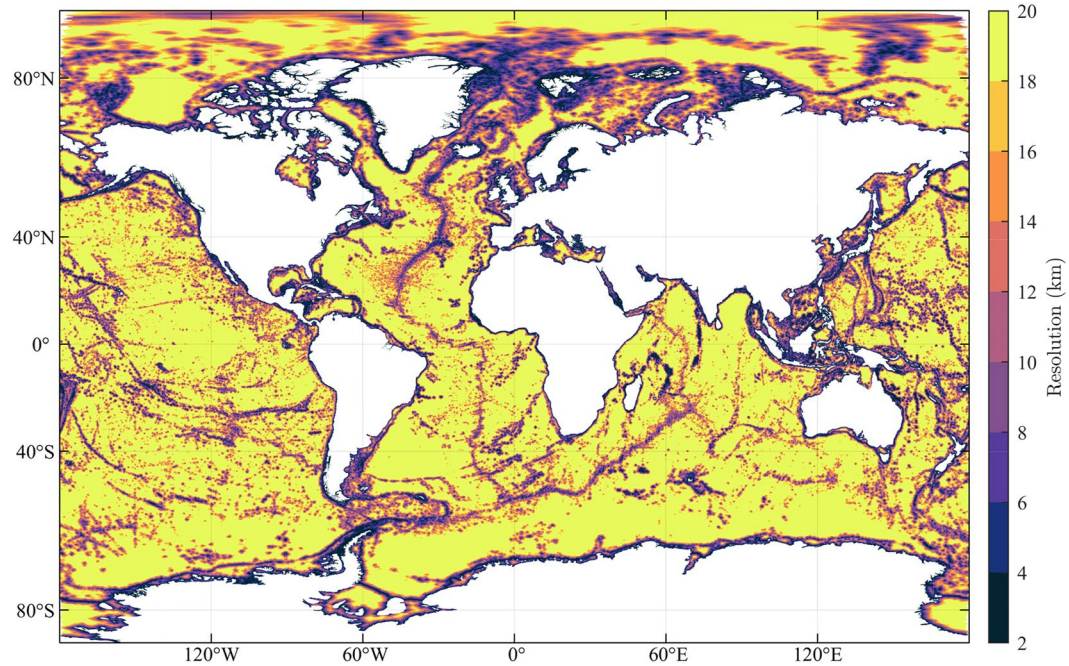

Figure 1. Resolution of the global mesh used in this study. Minimum resolution is 2 km, and maximum is 25 km.

2.4. ADCIRC Implementation

Simulations in this study were executed using version 55 of the ADCIRC model, a finite element-based 2-D/3-D shallow water equation (SWE) solver that considers the reformulation of the continuity equation into the Generalized Wave Continuity Equation (GWCE; Luettich & Westerink, 2004; Pringle et al., 2021). Several modifications were made in version 55 that enable the modeling of global domains and the use of larger time steps (Pringle et al., 2021). When processes are sufficiently resolved, ADCIRC introduces minimal numerical or artificial dissipation. By carefully selecting the temporal weighting parameter (τ_0) in the GWCE, it is possible to optimize numerical dispersion properties and better capture phases of tidal propagation (Atkinson, Westerink, & Hervouet, 2004; Atkinson, Westerink, & Luettich, 2004). For this model, a value of $\tau_0 = 0.027$ was used to satisfy stability constraints (Pringle et al., 2021). The time step for all simulations was 60 s.

Simulations were forced with the M_2, Q_1, O_1, P_1, K_1, N_2, S_2, and K_2 equilibrium tides. Tidal analysis was performed over a 180-day period with a 30-day spin up period to dampen any transients from the cold start of the model. For the perturbation runs described in Section 5, shorter runs of 45 days with a 15 day spin up were possible because the M_2 tide was the only constituent considered. The Smagorinsky coefficient, which controls lateral eddy viscosity (υ_t), was set to a value of 0.05 for all simulations. Results showed little to no sensitivity to the selection of υ_t.

2.5. Methods of Analysis

To evaluate both the amplitude and phase of the error in one metric, the root mean square discrepancy (D) was used (X. Wang et al., 2012):

$$D = \sqrt{0.5 \sum_k \left[\left(A_o^k\right)^2 + \left(A_m^k\right)^2 - 2A_o^k A_m^k \cos\left(\theta_o^k - \theta_m^k\right) \right]} \tag{7}$$

where A and θ are amplitude and phase, k denotes the kth constituent, o denotes observed amplitude/phase, and m denotes modeled amplitude/phase. This metric was calculated at the centroid of each element by interpolating TPXO9-atlas values (hereafter TPXO9) (Egbert & Erofeeva, 2002, 2021). TPXO9 was selected as the observed reference solution due to its high accuracy compared to tide gauges in open water regions (Stammer et al., 2014). All regions shallower than 20 m were omitted from the calculation of error metrics due to lower accuracy of

TPXO9 in coastal and inlet systems, inadequate resolution of complex inlet systems within our mesh, and lack of high resolution bathymetric data. To turn D into a single global metric, the area weighted mean of the discrepancy compared to TPXO9 $\left(\bar{D}_{tpxo}\right)$ was used:

$$\bar{D}_{tpxo} = \frac{\sum_i A_i D_i}{\sum_i A_i} \tag{8}$$

where A_i is the area of the ith element and D_i is the discrepancy at the centroid of the ith element.

In addition to computing the mean discrepancy to TPXO9, results were also compared to a compilation of global tide data sets derived from measured water level data (Pringle, 2017). Stations used for analysis were limited to ensure that they fell within the model domain and that sufficient resolution existed at their locations for an accurate analysis. A list of the specific stations used, as well as the amplitudes and phases from Pringle (2017) is available from Blakely (2021).

3. Dissipation Estimation

Total tidal energy dissipated was also estimated and compared to astronomical input and prior estimates of global tidal dissipation. This calculation was performed using velocity and elevation outputs at 30 min intervals over 180 days of simulation to find time averaged dissipation rates. The dissipation due to boundary layer friction and internal wave turbulence are found to be:

$$D_{bl} = \rho_0 C_d |\boldsymbol{u}|^3 \tag{9}$$

$$D_{it} = \rho_0 \boldsymbol{u} \cdot \boldsymbol{C} \cdot \boldsymbol{u} \tag{10}$$

where all variables have the same meanings as defined in Equations 1–3. In order to find total dissipation, these dissipation rates were time averaged and then integrated over the whole domain of the simulation. Thus, the total dissipation for boundary layer friction and internal tide generation are:

$$D_{bl,total} = \int_A \left[\frac{1}{T} \int_{t=t_0}^{t=t_f} D_{bl} dt \right] dA \tag{11}$$

$$D_{it,total} = \int_A \left[\frac{1}{T} \int_{t=t_0}^{t=t_f} D_{it} dt \right] dA \tag{12}$$

respectively. This method is different than that implemented in Egbert and Ray (2000, 2001), wherein the dissipation was calculated from a formula based on the balance between the so-called work rate and tidal energy flux using tidal amplitudes and volume fluxes. The advantage of using the parameterizations of stress to estimate dissipation is that it is possible to split the dissipation mechanisms clearly between internal tide conversion and boundary layer dissipation and ensure the positivity at all points in the model domain. In addition, this method allows us to pin point dissipation rates down to the mesh resolution scale.

4. Bathymetric Sensitivities

In order to understand the impact of bathymetry on tides, a selection of bathymetric data sets were applied to the mesh and 45-day tidal simulations were performed. This allows us to put into context the impact of frictional variability. All experiments used a directional C_{it} of 2.5 and a Manning's n of 0.022 $\mathrm{s\,m^{-1/3}}$ in the majority of the ocean and 0.028 $\mathrm{s\,m^{-1/3}}$ in the high dissipation regions defined in Section 5. We consider combinations of bathymetry from six different data sets as summarized in Table 1. Figure 2 shows the M_2 amplitude differences because of using various combinations of the bathymetric data sets.

Applying the GEBCO data sets requires careful consideration of their representation of the Arctic and Greenland ice shelves. Within GEBCO versions 2014, 2019, and 2020, altimeter data were used over these regions. Thus, any part of the mesh that was underneath the ice shelf was set to the minimum depth of 5 m in our model. Using the RTopo-2 data set allows us to estimate and interpolate onto our mesh the water column height between the ocean floor and the bottom of the ice sheet. It is especially important to have appropriate bathymetric values

Table 1
Summary of Bathymetric Data Sets and Combinations

Data set	Source	Resolution	Coverage
GEBCO 2014 Grid	GEBCO (2014)	30 arc-second	Global
GEBCO 2019 Grid	GEBCO (2019)	15 arc-second	Global
GEBCO 2020 Grid	GEBCO (2020)	15 arc-second	Global
CHS NONNA 100	CHS (2018)	100 m	Canadian Territorial Waters
RTopo-2	Schaffer et al. (2019)	30 arc-second	Greenland and Antarctica
nthaus100	Beaman (2018)	100 m	Northwest Australia/Timor Sea

Combination	Data sets included
I	GEBCO 2014 Grid
II	GEBCO 2014 Grid + RTopo-2
III	GEBCO 2019 Grid + RTopo-2
IV	GEBCO 2019 Grid + RTopo-2 + CHS NONNA 100
V	GEBCO 2019 Grid + RTopo-2 + CHS NONNA 100 + nthaus100
VI	GEBCO 2020 Grid + RTopo-2 + CHS NONNA 100 + nthaus100

under the Ronne Ice Shelf in the Weddell Sea. This region has been found to be a particularly powerful control on tides not only regionally but throughout the Atlantic Basin (Sulzbach et al., 2021; Wilmes & Green, 2014; X. Wang, Verlaan, et al., 2021). As Figure 2a shows, by properly treating the ice cavity, the effective length of the Atlantic Basin is increased, increasing wave propagation speed nearshore in the Weddell Sea and changing the wavelength of the resonant wave in the Atlantic. Arbic et al. (2009) demonstrate that, in resonant systems there is a "back effect" in the open ocean when key areas of tidal resonance are altered. This experiment corroborates the intrinsic resonance of the Atlantic basin.

A major difference between GEBCO (2014) and GEBCO (2019) is that the newer data set has twice the resolution. An additional difference is that GEBCO (2019) assimilates more high-resolution data sets including the Canadian CHS-NONNA100 and northwest Australian nthaus100 bathymetric data sets. While the use of GEBCO (2019) does not result in nearly the magnitude of response change as that from the inclusion of RTopo, it does significantly impact tides all over the globe as seen in Figure 2b. Throughout the Pacific, the response to using GEBCO (2019) rather than GEBCO (2014) is ±3 cm while in the Atlantic, it reaches as high as + 20 cm along the US East Coast. The large differences in the Atlantic can be attributed to the improved representation of bathymetry in GEBCO (2019) in the highly dissipative Hudson Bay system (consisting of Hudson Bay, the Hudson Strait, and the Foxe Basin). Previously Egbert and Ray (2001) demonstrated that the Hudson/Baffin Bay system was the most significant dissipation region globally and Arbic et al. (2009) demonstrated through their blocking experiments that Hudson Bay significantly impacted Atlantic tides. In Section 5, we pinpoint the dissipation region of most significance in the Hudson Bay system as the eastern portion of the Foxe Basin, followed by the Hudson Strait.

Due to the importance of correctly resolving the Hudson Bay system, the CHS-NONNA100 data set in its original 100 m resolution was independently interpolated onto the portion of the mesh within the CHS-NONNA100 coverage on top of the GEBCO (2019) data set. Figure 2c clearly shows that the higher resolution of using the original data set does have a noticeable effect. In the Arctic Ocean, the tidal response was a change in amplitude up to 2 cm. Additionally, the US East Coast is again impacted quite heavily, with a change of up to 3 cm in the Northeast.

Another region with high dissipation is the Timor Sea/Northwest Australia. In order to examine the effect that higher resolution bathymetry had in that region, the nthaus100-grid (Beaman, 2018) was interpolated directly onto our mesh on top of GEBCO (2019). This data set is at 100 m resolution and was also already up-scaled to coarser resolution in the GEBCO (2019) database. Figure 2d shows the response impact on the M_2 tide due to the direct inclusion onto our unstructured mesh of this bathymetry at higher resolution. Altering the bathymetry of the Timor Sea has modest nonlocal effects on tidal results.

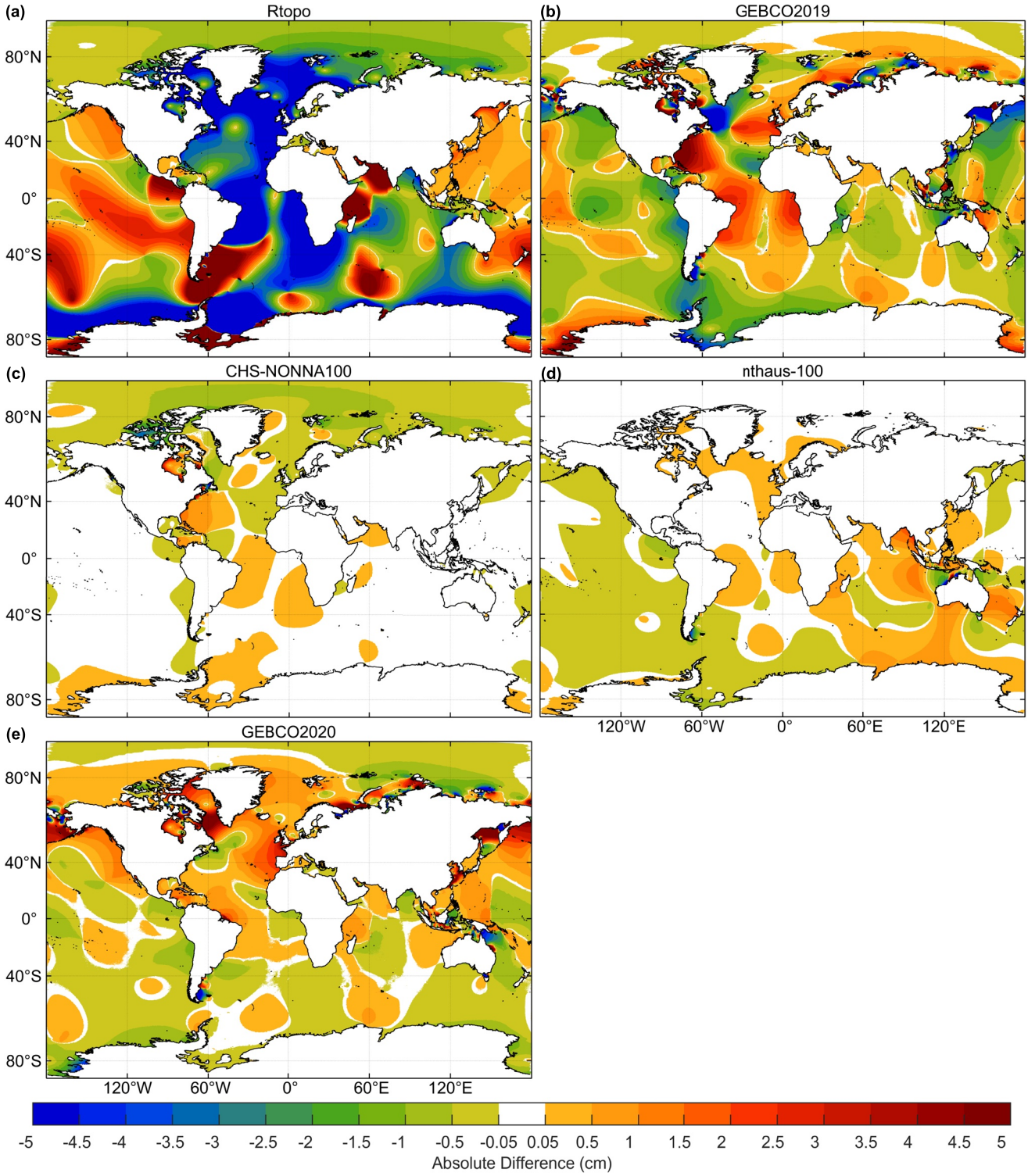

Figure 2. Changes in M_2 amplitude due to changes in bathymetry. Roman numerals refer to bathymetric combinations from Table 1. (a) II–I: Response to using RTopo under the Antarctic ice shelves. (b) III–II: Sensitivity from using GEBCO (2019) in place of GEBCO (2014). (c) IV–III: Response to using CHS-NONNA100 at its native resolution. (d) V–IV: Response to using nthaus-100 at its native resolution. (e) VI–V: Response to using GEBCO (2020) in place of GEBCO (2019).

Figure 2e shows that the updates to the GEBCO data set from GEBCO (2019) to the improved GEBCO (2020) resulted in substantial changes on global tides. Most heavily impacted are the Bering Sea, Hudson Bay, and the Ohkotsk Sea, all of which have responses over 5 cm in the M_2 tide.

Our bathymetric sensitivity investigation points to the significant impact that bathymetry can have on tides. This highlights the magnitude of improvement that bathymetric perturbations can have on tides, while also indicating that specific areas are far more critical than others for bathymetric accuracy. Regions, such as the Ronne Ice Shelf, the Weddell Sea, and the Hudson Bay system have impacts on global tides. In some situations the impact appears to be related to shifting resonant amplification while in others the impact appears to be related to dissipative controls as our frictional sensitivity studies will show. We note that altering bathymetry in specific regions can impact tides more than perturbing frictional processes. Combination VI provided the best solution of the various combinations of data sets and was used as the baseline for the rest of this study.

5. Sensitivity to Friction

5.1. Geographical Distribution of Dissipation

Using Equations 9–12, an analysis of dissipation within the model was performed by examining the dissipation within each element as well as the total tidal dissipation. Figures 3a and 3b show, on a log scale, the boundary layer and internal tide dissipation, respectively, of our model. Additionally, for reference, the maximum current speed and maximum tidal elevation are plotted in Figures 3c and 3d.

Figure 3a shows that the vast majority of the boundary layer dissipation within the model occurs in shallow regions near the coast. The areas of highest dissipation have a combination of shallow bathymetry, high velocities and large tidal amplitudes. Figures 4a, 4c, and 4e display the areas that account for 50%, 90%, and 99% of boundary layer dissipation. Ninety percentage of the boundary layer dissipation occurs in 1.4% of the surface area of the global ocean, highlighting the highly local nature of this dissipation mechanism. The high dissipation rate regions coincide well with previously published studies and include the Hudson Bay system, the European shelf, Georges Bank, the Bay of Fundy, the Patagonian shelf, the Northeast Brazilian shelf, and the Northwest Australian shelf (Egbert & Ray, 2001). Our study indicates the specific areas where dissipation is highly concentrated, including in the eastern portion of the Foxe Basin, Georges Bank, the Bay of Fundy, the English Channel, and the Strait of Dover suggesting that particular attention should be paid to resolving these portions of the physical system and correctly modeling local dissipation.

Internal tide dissipation is far less localized as can be seen in Figure 3b. Figures 4b, 4d, and 4f show the areas that account for 50%, 90%, and 99% of the internal tide dissipation in the model, respectively. Approximately 17.2% of the ocean accounts for 90% of the internal tide dissipation.

5.2. Global Sensitivity to Friction Parameters

Prior to examining the responses of tides to changes in localized friction parameters, we first studied tidal sensitivities to uniform change in friction parameters. In addition to better understanding the sensitivity to changes in globally constant friction parameters; this experiment also allowed us to compare different parameterizations of internal tide dissipation (directional vs. scalar C_{it}) and boundary layer dissipation (constant C_d or Manning's n). Due to boundary layer dissipation being highly localized, the majority of the model (mostly deep ocean and low velocity shelf regions) were left as commonly applied values for both C_d or Manning's n. Perturbing bottom friction values globally from standard values in most regions degrades local solutions without changing global error metrics. This is especially true across low energy shelves. Deep ocean friction values have little impact of tides as depths are large and currents are very small. In contrast, altering friction values in high energy dissipation zones has effects on a regional and basin scale. The internal tide parameter C_{it} was altered globally due to the far more widespread nature of this phenomenon.

5.2.1. C_d and Manning's n

Figure 5 shows the mean discrepancies compared to TPXO9 in various basins and marginal seas as a function of C_d or Manning's n. The deep and shallow water panels allow us to discern where the changes are most significant. Of particular note is how gentle the slopes of the mean discrepancy typically are. Changing bottom friction

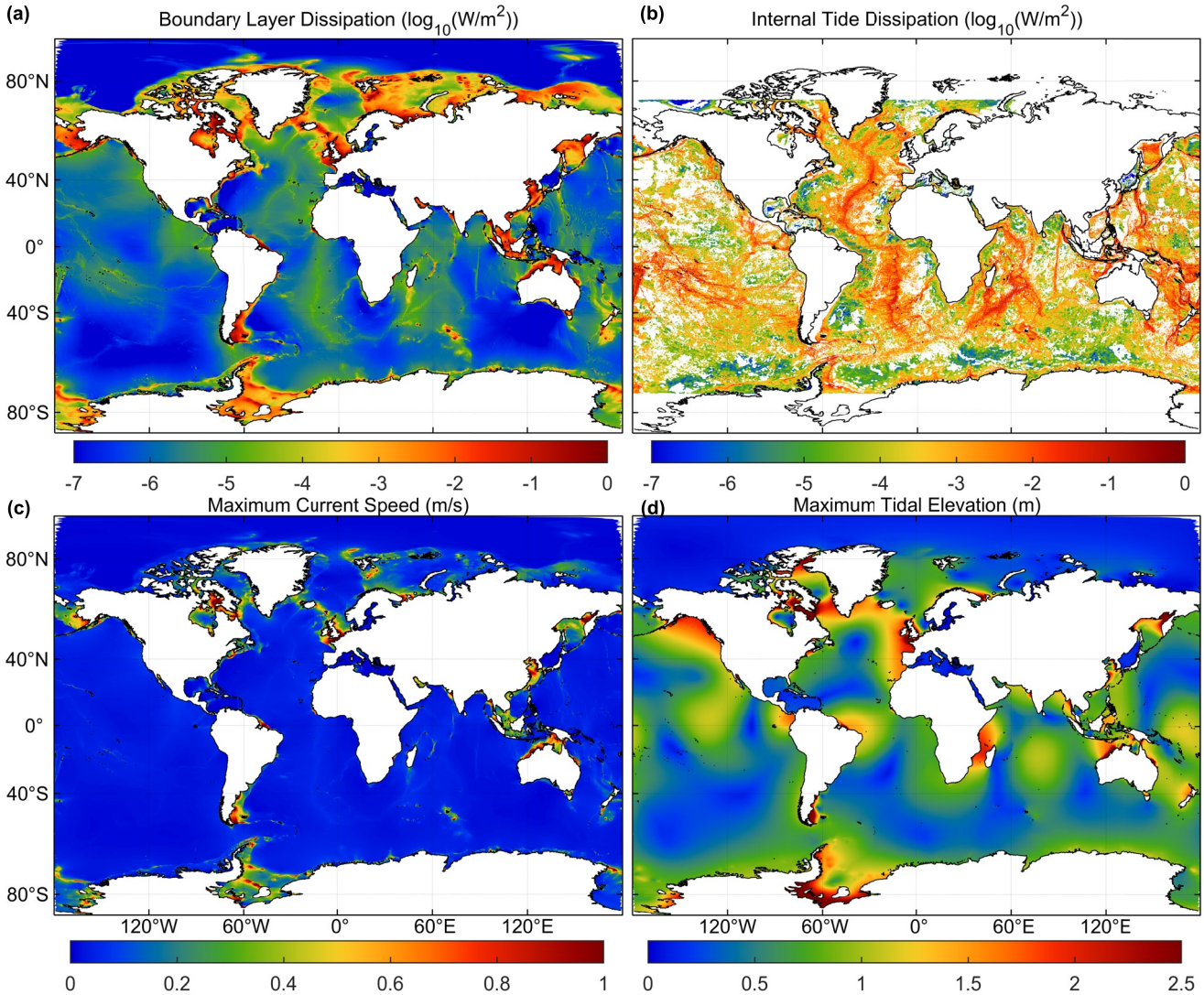

Figure 3. (a) Boundary layer dissipation. (b) Internal tide dissipation. (c) Maximum current speed. (d) Maximum tidal elevations.

globally does not have dramatic effects on the global tidal solution. However, certain regions such as the Yellow, Bering, and Java Seas are quite sensitive. The affected regions have large extents of shallow depths with highly energetic resonant tides and are therefore sensitive to local dissipation. Furthermore regional island chains—such as the Ryukyu and Aleutian Islands—with steep topographic gradients and shallow crests tend to converge flows across these submerged barriers at high current speeds leading to significant dissipation. We do note that due to the resolution provided and the inherent depth averaging, the model does not capture lateral and vertical eddying associated with the often very energetic flows passing across these barrier island chains. While lateral viscous terms may capture a portion of this dissipation, in our model with a 2-km limit on resolution, bottom friction and internal tide dissipation can serve as a mechanism to drain the missing energy associated with the unresolved eddy structures.

For the Manning scheme, the majority of regions have relatively consistent minima at Manning values ranging from 0.026 to 0.030, while the Yellow Sea requires lower friction than the rest of the globe. The fine, silty substrate in the Yellow Sea means that lower values for bottom friction parameters are more optimal, explaining physically why this particular area has a minimum at a lower bottom friction coefficient than other regions. This finding is consistent with previous studies that showed small bottom friction coefficients required in the Yellow Sea (Lefèvre et al., 2000; Pringle et al., 2018; Qian et al., 2021). Unlike the Manning scheme, there is not quite

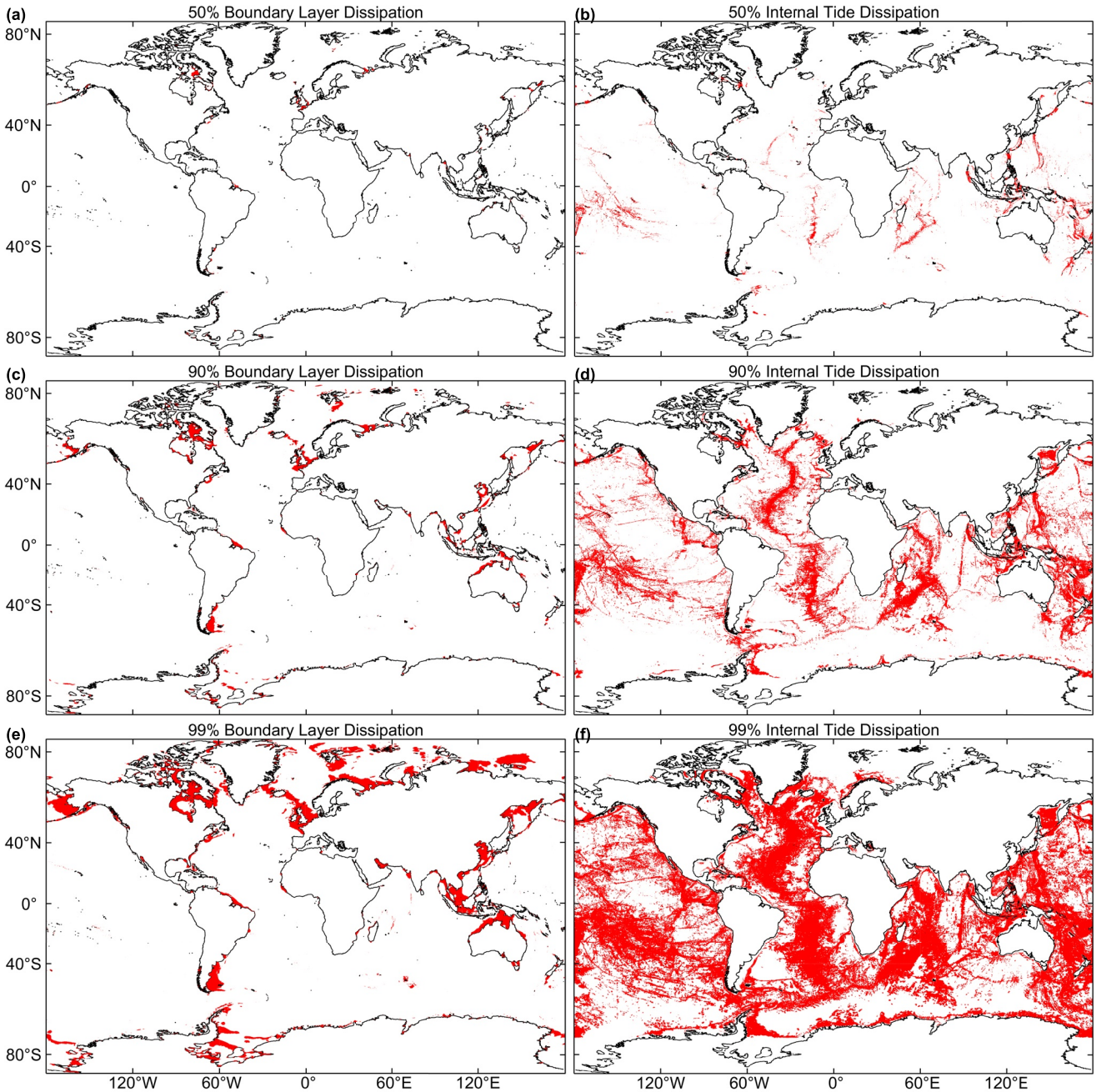

Figure 4. (a), (c), and (e) show the areas that account for 50%, 90%, and 99% of dissipation within the Advanced Circulation Ocean Model. The corresponding area ratios are 0.2%, 1.4%, and 4.3% of the model area, respectively. (b), (d), and (f) show the same for internal tide dissipation with the area ratios being 2.3%, 16.7%, and 45.6% of the model area. Dissipation rates were interpolated to the centroids of each element. Elements were then sorted by the dissipation rate in descending order and total dissipation per element was estimated via integration. In this manner, it was possible to find the least area that could account for 50%, 90%, and 99% of the total model dissipation.

as much consistency in where the minima occur for the different regions in the C_d scheme. Instead, for example, the NE Pacific gets the best results at $C_d \approx 3.3 \times 10^{-3}$ while for the North Atlantic, $C_d \approx 1.9 \times 10^{-3}$ yields the best results.

From the numerical experiments described above, we prefer the Manning parameterization largely due to the minimum error for most basins and marginal seas (the Yellow Sea being the exception) having the lowest error at approximately $n = 0.028$. This is in contrast to the C_d parameterization where the improvement is much less

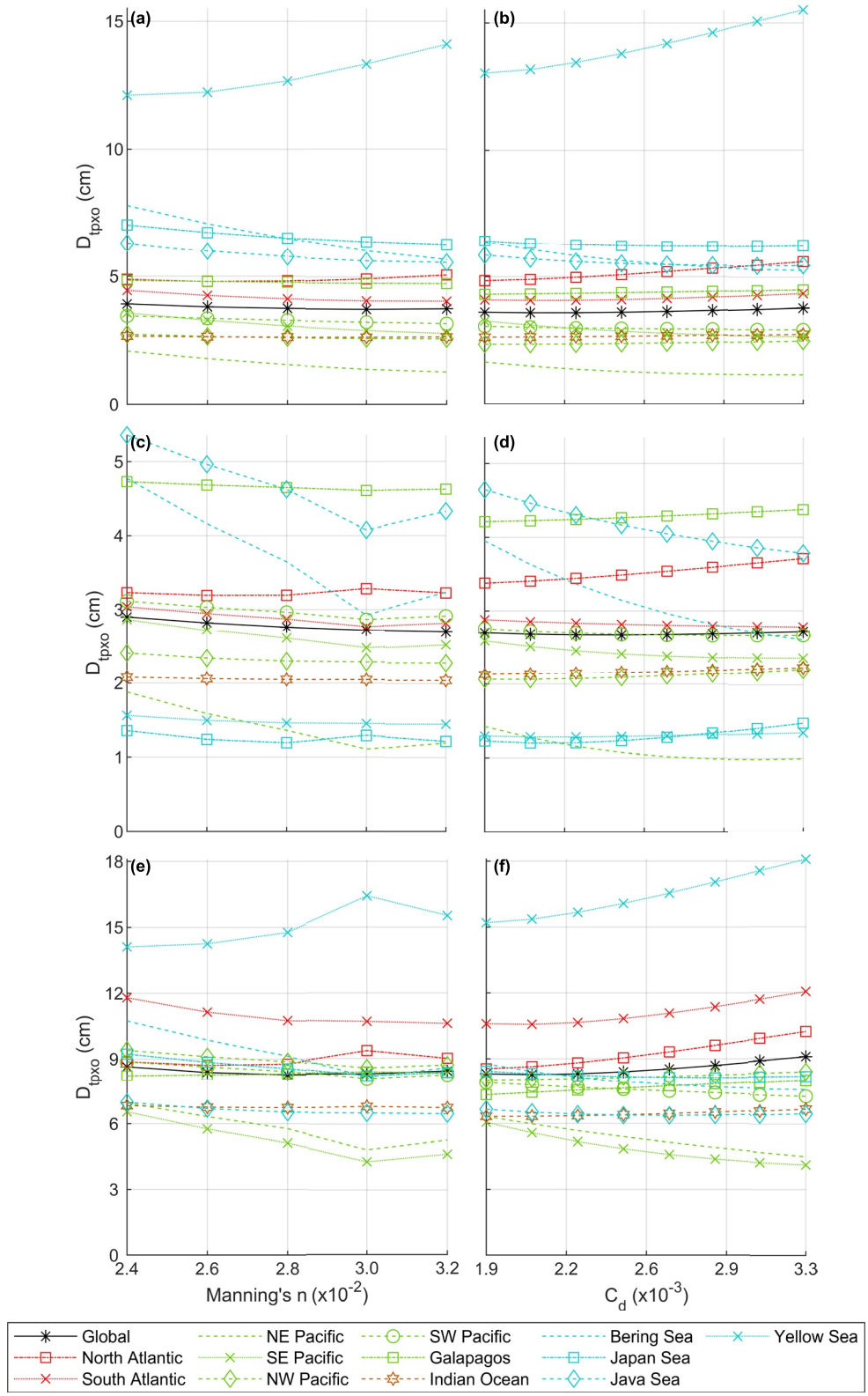

Figure 5. Comparisons of the mean discrepancy compared to TPXO9 M_2 tide as a function of varying Manning's n (on left) and constant friction coefficient (on right). (a) and (b): Overall mean discrepancy. For this study, areas shallower than 20 m were omitted from analysis. (c) and (d) Deep mean discrepancy. Deep is defined as anything deeper than 1,000 m (e) and (f) Shallow mean discrepancy. Shallow is defined as anything between 20 and 1,000 m deep.

consistent. We also note that Manning's n specified on continental shelves leads to a much better generation and propagation of hurricane forerunners associated with wind-generated shore parallel currents and the resulting geostrophic set up (Hope et al., 2013; Kennedy et al., 2011). The extra depth dependency in the Manning's n formulation redistributed resistance to the inner shelf (and inland waterbodies) from the outer and mid shelf as compared to depth independent bottom drag coefficients.

5.2.2. Directional and Scalar C_{it}

Similar to the investigation of various bottom friction parameterization, we studied the performance of the directional and scalar forms of the internal tide parameterization by varying the parameter C_{it}. Figure 6 shows the responses in mean discrepancy of the model compared to TPXO due to changing C_{it} values. The effects, especially in overall (Figures 6a and 6b) and deep water (Figures 6c and 6d) are larger than those of altering boundary layer dissipation. Most notably, the scalar parameterization of C_{it} is highly sensitive in all basins and has a much larger impact than the directional parameterization. The Bering Sea has a large sensitivity to internal tide dissipation (except in shallow Bering shelf waters for the directional case) regardless of the parameterization used due to high flow rates creating internal drag across the topographically steep Aleutian Islands.

Of particular note is the steepness of the curves in Figure 6 compared to the curves in Figure 5. While bottom friction could change results by only up to a centimeter in the most drastic cases, altering C_{it} changes results in several centimeters even in the least affected regions. We note that regions that are strongly affected by bottom friction are similarly affected by C_{it}. The Yellow Sea shows the same degradation of solution with higher C_{it} as it did with the higher bottom friction coefficient. The marginal seas exhibit much more sensitivity to friction regardless of the dissipation mechanism.

While the steeper curves of the scalar parameterization could result in simpler optimization, the directional model is more physically intuitive because it produces dissipation only when flow crosses steep topographic gradients. Based on the mechanisms by which internal waves are generated, this is more consistent. Furthermore, the overall mean discrepancy in the directional model was lower than the overall mean discrepancy in the scalar parameterization.

5.2.3. Global Baseline Model

Based on the experiments described, we concluded that the best methodology for examining localized sensitivity to friction was to select the Manning's n and directional C_{it} parameter that provided the lowest error with constant parameters when compared to TPXO9. A Manning's n of 0.028 $s\,m^{-1/3}$ in the regions of high dissipation discussed in Section 5.3.1 and 0.022 $s\,m^{-1/3}$ elsewhere, in combination with a C_{it} value of 2.5 with the directional parameterization were selected as baseline starting values. The mean discrepancy compared to TPXO9 of this model for the M_2 constituent was 2.81 cm for waters deeper than 1,000 m, 7.94 cm for regions between 20 and 1,000 m, and 3.70 cm overall.

5.3. Local Sensitivity to Friction Parameters

Based on the global baseline established, we further investigate areas that are particularly sensitive to local perturbations in both boundary layer and internal tide coefficients. To facilitate these experiments, continental shelves as defined by Harris et al. (2014) were divided into 60 regions and individually had Manning's n perturbed by 0.002. For internal tide dissipation, 12 individual regions were created, which broadly capture unique topography, and C_{it} was perturbed by 0.2 using a directional parameterization.

5.3.1. Sensitivity to Bottom Friction

Bottom friction regions were selected based on knowledge of the geomorphology of the ocean floor, and guided by regions of high boundary layer dissipation. The vast majority of regions perturbed showed only local changes in M_2 amplitude when the bottom friction is changed. Figures 7c and 7d show two examples of this. These highly local responses are in regions with relatively low tidal velocities and are often within larger bays or inlet systems. These types of perturbation responses are often very small, with magnitudes only up to 0.2 cm.

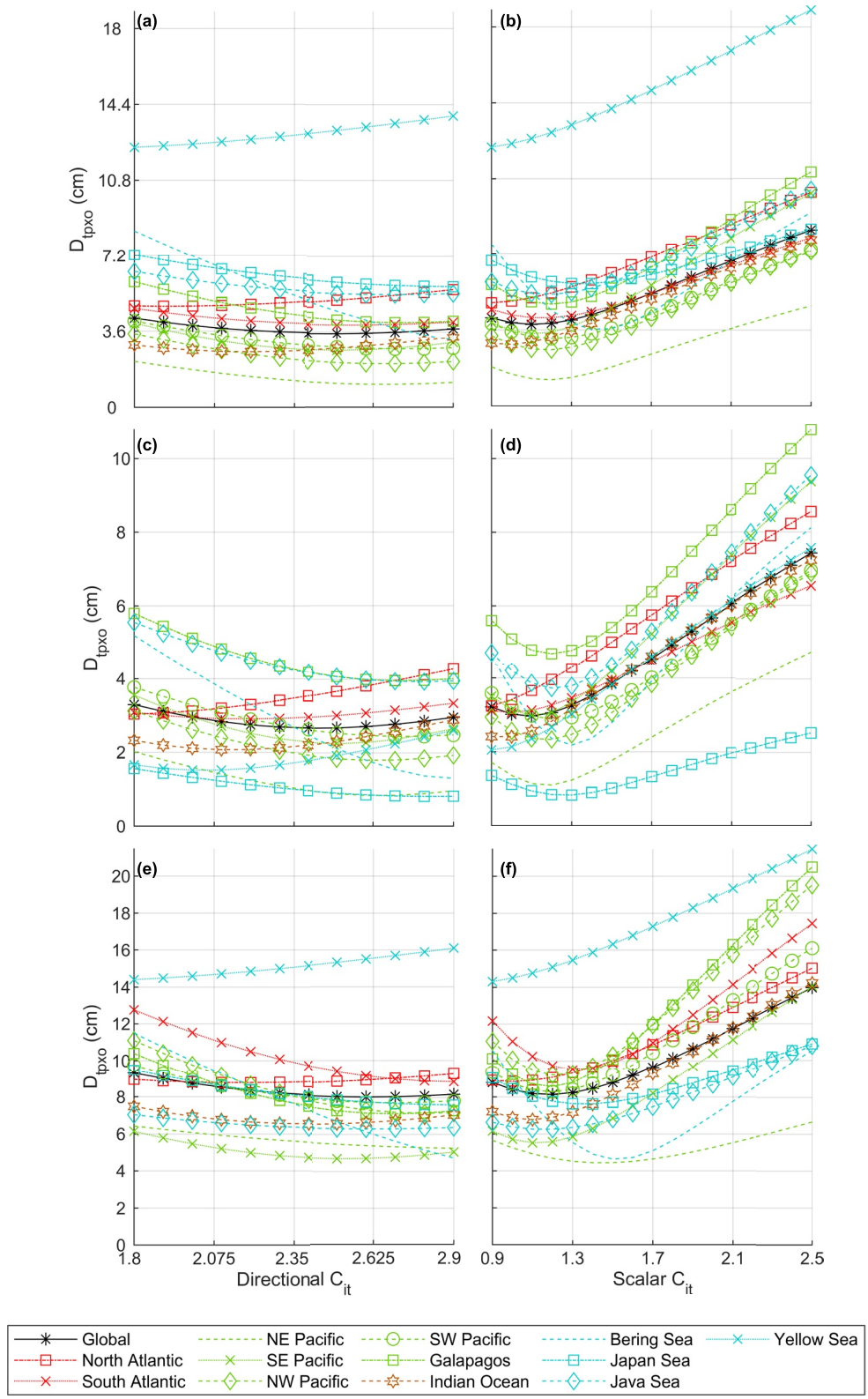

Figure 6. Comparisons of the mean discrepancy compared to TPXO9 of the M_2 tide as a function of varying C_{it} with a directional parameterization (on left) and a scalar parameterization (on right). (a) and (b) Overall mean discrepancy. For this study, areas shallower than 20 m were omitted from analysis. (c) and (d) Deep mean discrepancy. Deep is defined as anything deeper than 1,000 m (e) and (f) Shallow mean discrepancy. Shallow is defined as anything between 20 and 1,000 m deep.

Another common response seen is a "regional" response. Figure 7f shows the response of the tides to raising friction on the West Florida Shelf. In this case, there is a noticeable response away from the shelf in question, with a response on the west and north sides of the Yucatan Peninsula as well as some change in the Straits of Florida. Unlike the Louisiana/Texas shelf (Figure 7d) and the Gulf of Aden/Red Sea (Figure 7c), the West Florida shelf experiences relatively high tidal velocities due to shelf resonance. By altering the dissipation within that region, the dynamics within the Gulf of Mexico are changed. Similar responses can be seen in Cook Inlet (Figure 7b), which has a large tidal range and is a key dissipator in Alaska, resulting in perturbation responses within the adjacent Shelikof Strait and even in the distant Bristol Bay; the Arafura Sea (Figure 7a), which is surrounded by complex island systems and channels with resonant high velocities impacts the Java Sea, Gulf of Carpentaria, and even extending up to the Sulu Sea and the West Australian Shelf; and the Sea of Japan (Figure 7e), where raising the friction in the Korean Strait results in a large response within the Yellow Sea. This is not a comprehensive list of regional or highly local responses but rather gives examples of some regions where such responses can be seen.

Figure 8 shows the effect of perturbing the bottom friction in regions with significant, basin-scale impacts, including the Hudson Bay system, Baffin Bay (incorporating a portion of the Hudson Strait), Georges Bank, and the European Shelf. High boundary layer dissipation regions are typically quite sensitive to bottom friction perturbations, impacting regions away from the perturbed region. Conversely, low boundary layer dissipation results in insensitivity to changes in bottom friction.

One particularly interesting region is Georges Bank. This oval-shaped relief feature off the coast of Massachusetts is approximately 250 km long and 120 km wide, accounting for less than a tenth of a percent of the total ocean area. It is significantly shallower than the surrounding ocean and the rest of the Massachusetts Bay, with depths ranging from approximately 15 to 70 m. As Figure 3a shows, Georges Bank has very high boundary layer dissipation owing to its shallow depths, high velocity flows, and rough bottom and scoured sediments. Changing the bottom friction on Georges Bank affects the M_2 amplitude all along the East Coast of the United States, in the west Caribbean, and even off the coasts of Brazil and in the Gulf of Guinea as seen in Figure 8c. While some other regions have similar extent of response to perturbations, all of them are significantly larger in area than Georges Bank.

Most areas with this high sensitivity have a number of things in common. Foremost among these are high dissipation rates. While the regions used in their calculations are not identical to those used in this study, there is significant overlap in what Egbert and Ray (2001) found to be the largest tidal dissipators and regions found to be highly sensitive to bottom friction in this study. For example, the largest shallow water tidal dissipator they found was the Hudson Bay (in their study, the Hudson Bay region also included Baffin Bay, the Labrador Sea, and the Northwest Passage). In this study, two of the largest responses to perturbing Manning's n are in the Hudson Bay (Figure 8a)—incorporating the western Hudson Strait and the Foxe Basin—and Baffin Bay—incorporating the eastern end of the Hudson Strait and Ungava Bay (Figure 8b). Raising the friction in these two regions has an effect throughout the North Atlantic, lowering tides along the East Coast of the United States and raising them in Western Europe and North Africa. This impact correlates very well with the critical dissipation regions defined in Figure 3.

Another region known to be a large tidal dissipator is the European Shelf. Again, the response to raising friction within this highly dissipative area is basin-scale. Figure 8e shows how altering friction on the European Shelf alters the M_2 tide throughout the North Sea, the North Atlantic, and even within the Gulf of Guinea and the northern Mozambique Channel. The Patagonian Shelf (Figure 8f), Eastern Australia (Figure 8h), and the Bay of Fundy (Figure 8d) also make both the list of large tidal dissipators and highly sensitive regions that impact tidal solutions far from the region where friction was perturbed.

Because there are a limited number of regions that have large-scale effects when perturbed, only select bottom friction regions were considered in the optimization. While local results might improve by changing bottom friction in, for example, the Puget Sound, it would have little to no effect globally. As such, regions that were highly sensitive, as well as a few that are of interest for future work, were selected. These regions are listed in Table 2 and their extent is shown in Figure 9.

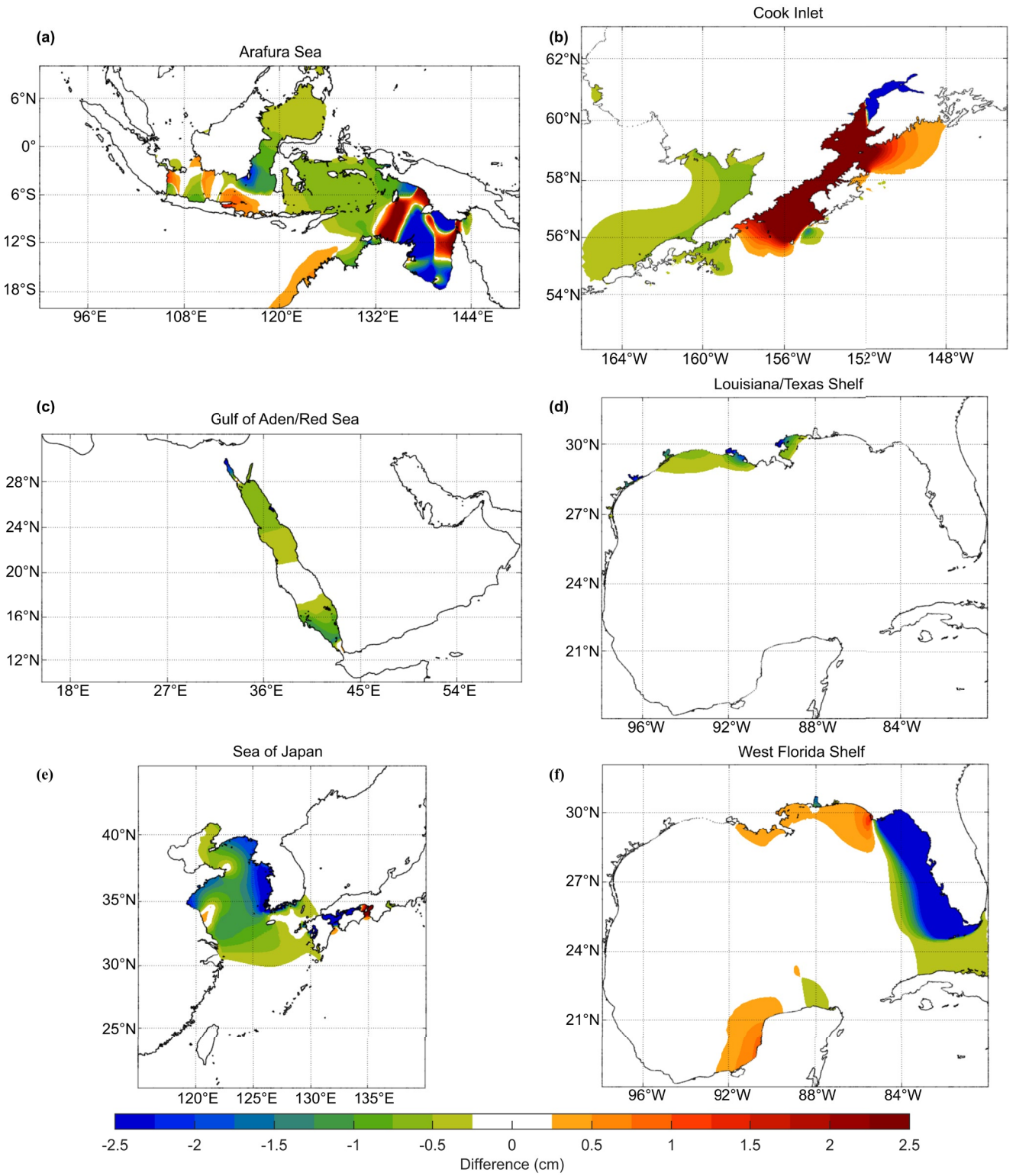

Figure 7. Response of the M_2 amplitude to raising the Manning's n by 0.002 $s\,m^{-1/3}$ in selected regions. (c) and (d) are examples of highly local responses, that is, the response is confined almost entirely to the region with perturbed friction. (a), (b), (e), and (f) show region-scale responses, with responses not necessarily confined to the region with perturbed friction but not nearly on a basin-scale.

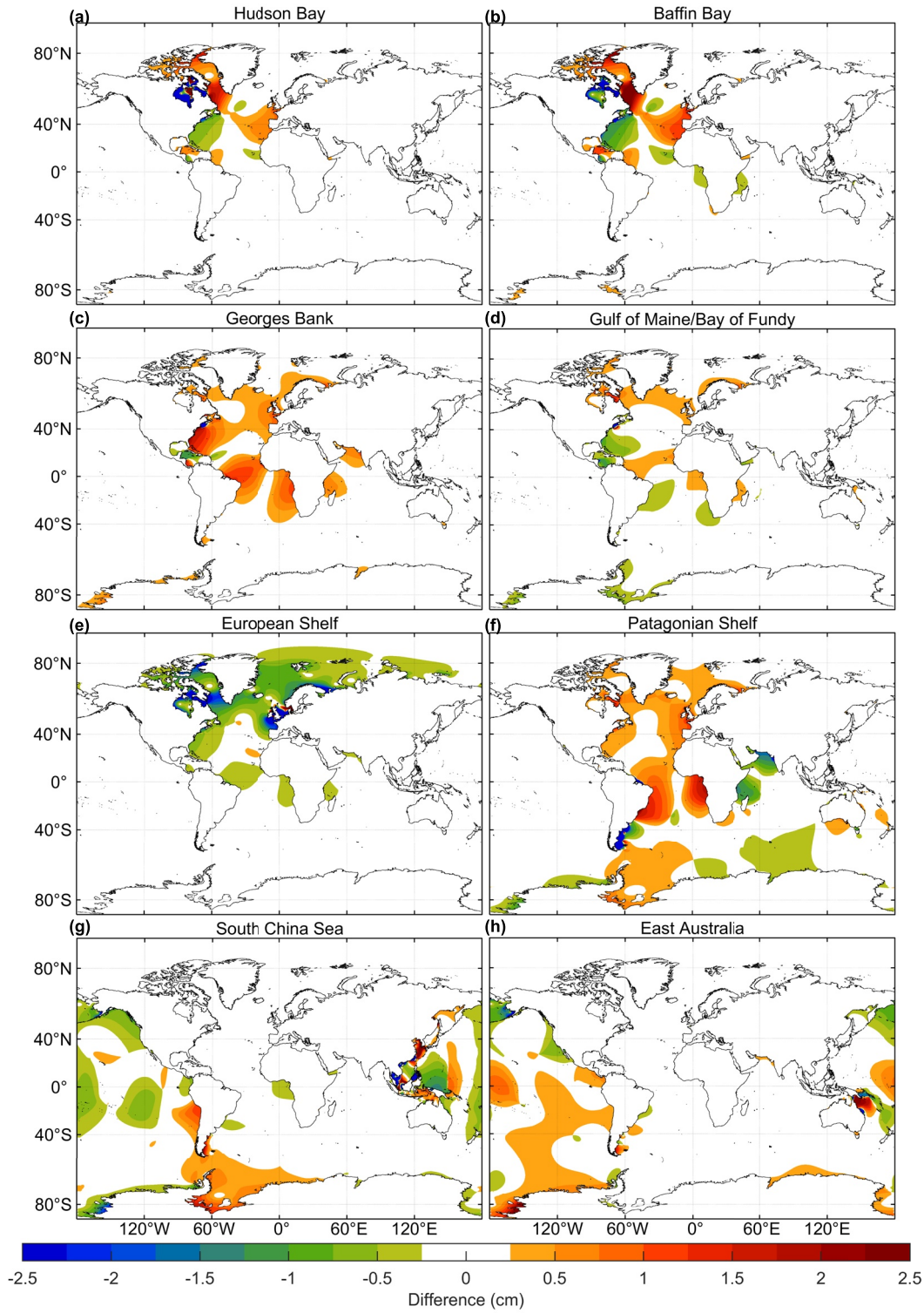

Figure 8. Examples of basin-scale responses in the M_2 amplitude due to perturbing Manning's n by 0.002 $s\,m^{-1/3}$ in certain regions.

5.3.2. Sensitivity to the Coefficient of Internal Tides

Figure 10 shows the geographic extent of the internal tide friction regions. Each defined region was selected to broadly characterize unique physical characteristics of the ocean basins. The Pacific and Atlantic oceans were

Table 2
Manning's n ($sm^{-1/3}$) for Regions of Interest for Progression of Runs

Region	Global baseline	Global optimization	Local re-optimization
Aleutian Islands*[1]	0.028	0.037	0.087
Arabian Sea/Persian Gulf	0.028	0.018	0.021
Arctic Ocean	0.028	0.042	0.042
Baffin Bay	0.028	0.027	0.027
Bass Strait	0.028	0.018	0.025
Bering Sea*[1]	0.028	0.037	0.025
East Australian Shelf	0.028	0.018	0.018
East China Sea*[2]	0.028	0.026	0.010
English Channel*[3]	0.028	0.033	0.026
European Shelf*[3]	0.028	0.033	0.026
Georges Bank	0.028	0.033	0.033
Gulf of Maine/Bay of Fundy	0.028	0.035	0.035
Gulf of St. Lawrence	0.022	0.018	0.018
Hudson Bay	0.028	0.029	0.029
Irish Sea*[3]	0.028	0.033	0.026
Java Sea/Gulf of Thailand	0.028	0.041	0.036
Korean Strait*[2]	0.022	0.022	0.015
Northwest Passage	0.028	0.048	0.048
North Australian Shelf	0.028	0.023	0.023
Patagonian Shelf*	0.028	0.025	0.031
Ryuku Islands*[2]	0.028	0.026	0.099
Salish Sea*[4]	0.022	0.022	0.022
Sea of Japan*[2]	0.022	0.022	0.046
Sea of Ohkotsk	0.028	0.030	0.030
South China Sea	0.028	0.041	0.040
Southwest Australian Shelf	0.028	0.023	0.023
Strait of Georgia/Puget Sound*[4]	0.022	0.022	0.022
West Florida	0.022	0.029	0.034
Yellow Sea	0.028	0.023	0.020

Note. Asterisks denote regions that, following the global optimization, were re-optimized locally. Numbers denote regions that were subdivided following the global optimization.

divided into multiple regions due to their large extent with the Galapagos being separated from the rest of the Pacific due to large submerged mountain chains. Marginal seas were separated due to the steep bathymetric gradients and large island chains in those regions.

Figure 11 shows the responses to perturbing C_{it} in select regions. With the exceptions of the Bering Sea (Figure 11j), the Japan and Ohkotsk Seas, and the East China/Yellow Sea, all of the C_{it} regions had responses to the perturbation that were more far reaching than even the most nonlocal Manning perturbation. More importantly, there is significant overlap between the regions impacted by regional perturbations, with for example, the response impact to perturbing C_{it} in the North Atlantic and the response impact to perturbing C_{it} in the South Atlantic dominantly overlapping. Clearly, the optimization of internal tide coefficients is a highly coupled problem.

There are a number of intriguing observations to be made about the responses to altered internal tide friction seen in Figure 11. First, there is notable similarity between the sensitivity in the North Atlantic (Figure 11a) and South Atlantic (Figure 11b). The South Atlantic has more of an effect outside of the Atlantic Basin, especially in the Indian Ocean and along the West Coast of the Americas; within the Atlantic, there is remarkable consistency. Additionally, within the Pacific Ocean, the Southwest (Figure 11e) and Northeast (Figure 11d) perturbations have had a larger effect than the Southeast (Figure 11f) and Northwest (Figure 11c). Additionally, the Galapagos region (Figure 11g) has significant effect.

While the Bering Sea, Japan and Ohkotsk Seas, and the East China/Yellow Sea all had largely local effects, they were included as separate regions despite their relative insensitivity globally. By optimizing the C_{it} within these marginal seas, results could be improved regionally by better capturing local physics.

6. Global Optimization

6.1. Optimization of Parameters

In order to optimize both the internal tide and Manning's n parameters, it is useful to treat the complex amplitude at a point in the model as the baseline complex amplitude plus the changes in amplitude due to the alteration of friction factors in various locations. This allows for relative simplicity in predicting what tidal results will be without performing hundreds of tidal simulations. We will use the following definitions:

$$Z^k_{o,m} = Re^k_{o,m} + iIm^k_{o,m} \tag{13}$$

$$Z^k_{b,m} = Re^k_{b,m} + iIm^k_{b,m} \tag{14}$$

$$f^k_m(\boldsymbol{x}) = g^k_m(\boldsymbol{x}) + ih^k_m(\boldsymbol{x}) \tag{15}$$

where $Z^k_{o,m}$ is the observed complex amplitude composed of real (Re) and imaginary (Im) parts interpolated from TPXO9 of constituent k at centroid m and i denotes the imaginary unit ($i^2 = -1$). Similarly, $Z^k_{b,m}$ is the complex amplitude of constituent k at node m in the baseline run from which the perturbations are made; $f^k_m(\boldsymbol{x})$ is the complex-valued real function that describes the changes in complex amplitude of constituent k at node m as a function of the change in friction factor vector $\boldsymbol{x}$ in the M regions of interest. f^k_m is further decomposed into the real valued functions $g^k_m(\boldsymbol{x})$ and $h^k_m(\boldsymbol{x})$. Both g^k_m and h^k_m can be written as the summation of functions $g^k_{j,m}(x_j)$ and $h^k_{j,m}(x_j)$, which are the changes at node m of the kth constituent of the real and imaginary components due the altering friction in region j. This results in:

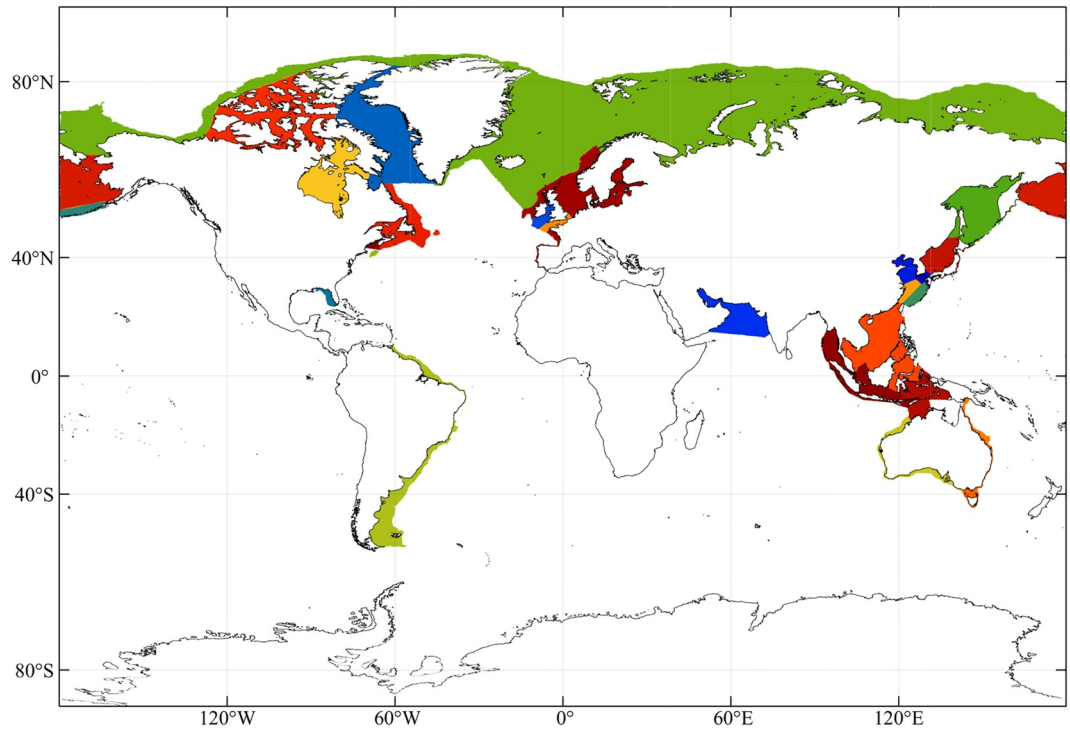

Figure 9. Boundary layer dissipation regions selected for use in the global optimization. Most areas were chosen due to the basin-scale response to frictional perturbation. Some—including the West Florida Shelf and the Gulf of St. Lawrence—were selected due to future work focused on those areas.

$$g_m^k(\boldsymbol{x}) = \sum_{j=1}^{M} g_{j,m}^k(x_j) \tag{16}$$

$$h_m^k(\boldsymbol{x}) = \sum_{j=1}^{M} h_{j,m}^k(x_j) \tag{17}$$

With Equations 13–17, the so-called cost function can be defined as the absolute value of the difference between the observed and modeled complex amplitudes—where the modeled amplitude is $Z_{m,i}^k = Z_{b,i}^k + f_i^k(\boldsymbol{x})$:

$$E_i^k(\boldsymbol{x}) = \sqrt{\left(Z_{o,i}^k - Z_{b,i}^k - f_i^k\right)\left(Z_{o,i}^k - Z_{b,i}^k - f_i^k\right)^*} \tag{18}$$

$$\begin{aligned} E_i^k(\boldsymbol{x}) &= \left(\left[\left(Re_{o,i}^k - Re_{b,i}^k - g_i^k(\boldsymbol{x})\right) + i\left(Im_{o,i}^k - Im_{b,i}^k - h_i^k(\boldsymbol{x})\right)\right] * \right. \\ &\quad \left.\left[\left(Re_{o,i}^k - Re_{b,i}^k - g_i^k(\boldsymbol{x})\right) - i\left(Im_{o,i}^k - Im_{b,i}^k - h_i^k(\boldsymbol{x})\right)\right]\right)^{\frac{1}{2}} \\ E_i^k(\boldsymbol{x}) &= \left(\left(Re_{o,i}^k - Re_{b,i}^k - g_i^k(\boldsymbol{x})\right)^2 + \left(Im_{o,i}^k - Im_{b,i}^k - h_i^k(\boldsymbol{x})\right)^2\right)^{\frac{1}{2}} \end{aligned} \tag{19}$$

To create a global cost function, sum over all the constituents $k = 1$ to L and all the elements $i = 1$ to N:

$$E(\boldsymbol{x}) = \sum_{i=1}^{N}\sum_{k=1}^{L} E_i^k(\boldsymbol{x}) \tag{20}$$

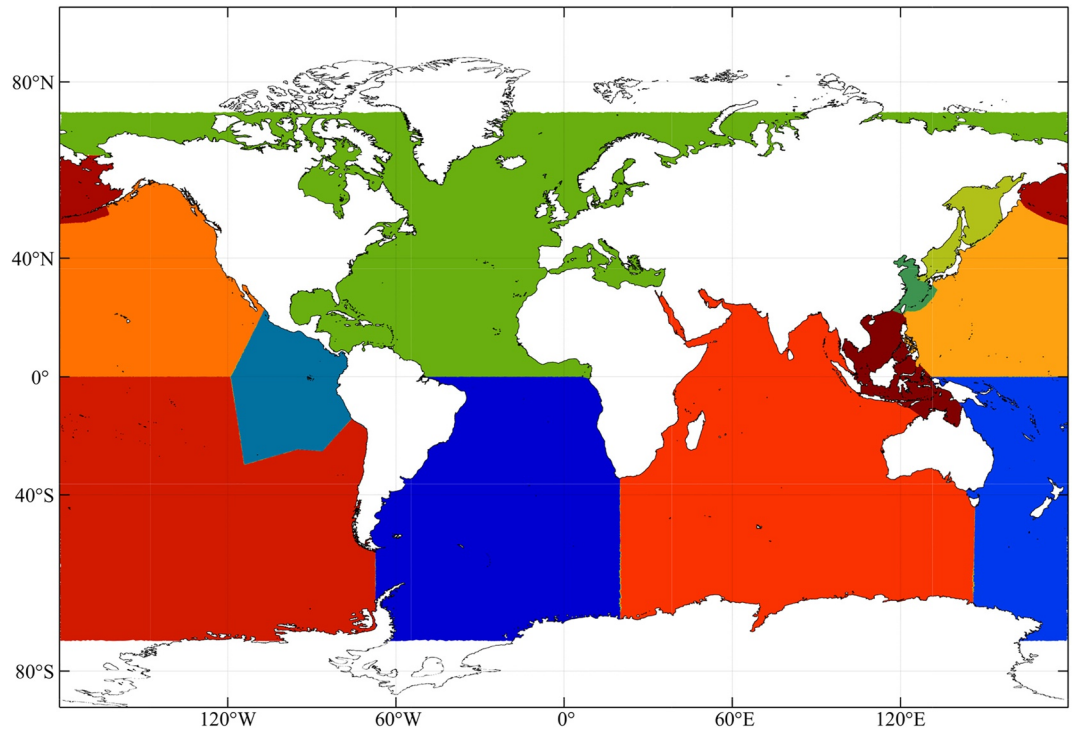

Figure 10. C_{it} regions used for optimization. A full list of region names can be found in Table 3. An important note is that NE Pacific is the region bound in the south by the equator, in the east by the prime meridian, and on the north and west by the Bering, Ohkotsk, Japan, and South China Seas. Similarly the SE Pacific is south of the equator, west of the prime meridian, and east of the Indian Ocean. NW Pacific is north of the equator, east of the prime meridian, and west of the west coast of North America. SW Pacific is south of the equator, east of the prime meridian, and west of South America.

Expand $g_i^k(\boldsymbol{x})$ and $h_i^k(\boldsymbol{x})$ as Taylor series and linearize:

$$g_i^k(\boldsymbol{x}) \approx g_i^k|_{\boldsymbol{x_0}} + \nabla g_i^k|_{\boldsymbol{x_0}} (\boldsymbol{x} - \boldsymbol{x_0}) \tag{21}$$

$$h_i^k(\boldsymbol{x}) \approx h_i^k|_{\boldsymbol{x_0}} + \nabla h_i^k|_{\boldsymbol{x_0}} (\boldsymbol{x} - \boldsymbol{x_0}) \tag{22}$$

Finally, let $\boldsymbol{x_0} = 0$ and the cost function becomes

$$E(\boldsymbol{x}) = \left[\sum_{i=1}^{N} \sum_{k=1}^{L} \left(\left(Re_{o,i}^k - Re_{b,i}^k - \nabla g_i^k|_{\boldsymbol{x_0}} \boldsymbol{x} \right)^2 + \left(Im_{o,i}^k - Im_{b,i}^k - \nabla h_i^k|_{\boldsymbol{x_0}} \boldsymbol{x} \right)^2 \right)^{\frac{1}{2}} \right] \tag{23}$$

Given all of the perturbations from Section 5 and this cost function, it is possible to find the combination of parameters that will minimize the error in the domain. For this study, MATLAB's fmincon function was used, which utilizes an interior point algorithm to find the minimum of a multidimensional function with constraints (MATLAB, 2018). Initially, limits were set to accepted ranges of values, with C_{it} bound between 1.0 and 4.0 and Manning values bound between 0.018 and 0.050 $\mathrm{s\,m^{-1/3}}$ to keep values relatively close to those tested as global values.

6.2. Optimized Parameters

The optimization of frictional parameters occurred in two parts. First, comparing to TPXO9, the M_2 amplitude at the centroid of all elements in the mesh with bathymetric depth greater than 20 m were considered. Equation 23 was minimized at each of these centroids for the dominant M_2 constituent. To reduce localized errors, the cost function minimization was locally reapplied to optimize the Manning's n within regions that had degraded during the global optimization. This was applied selectively in areas with particularly bad solutions and was only done

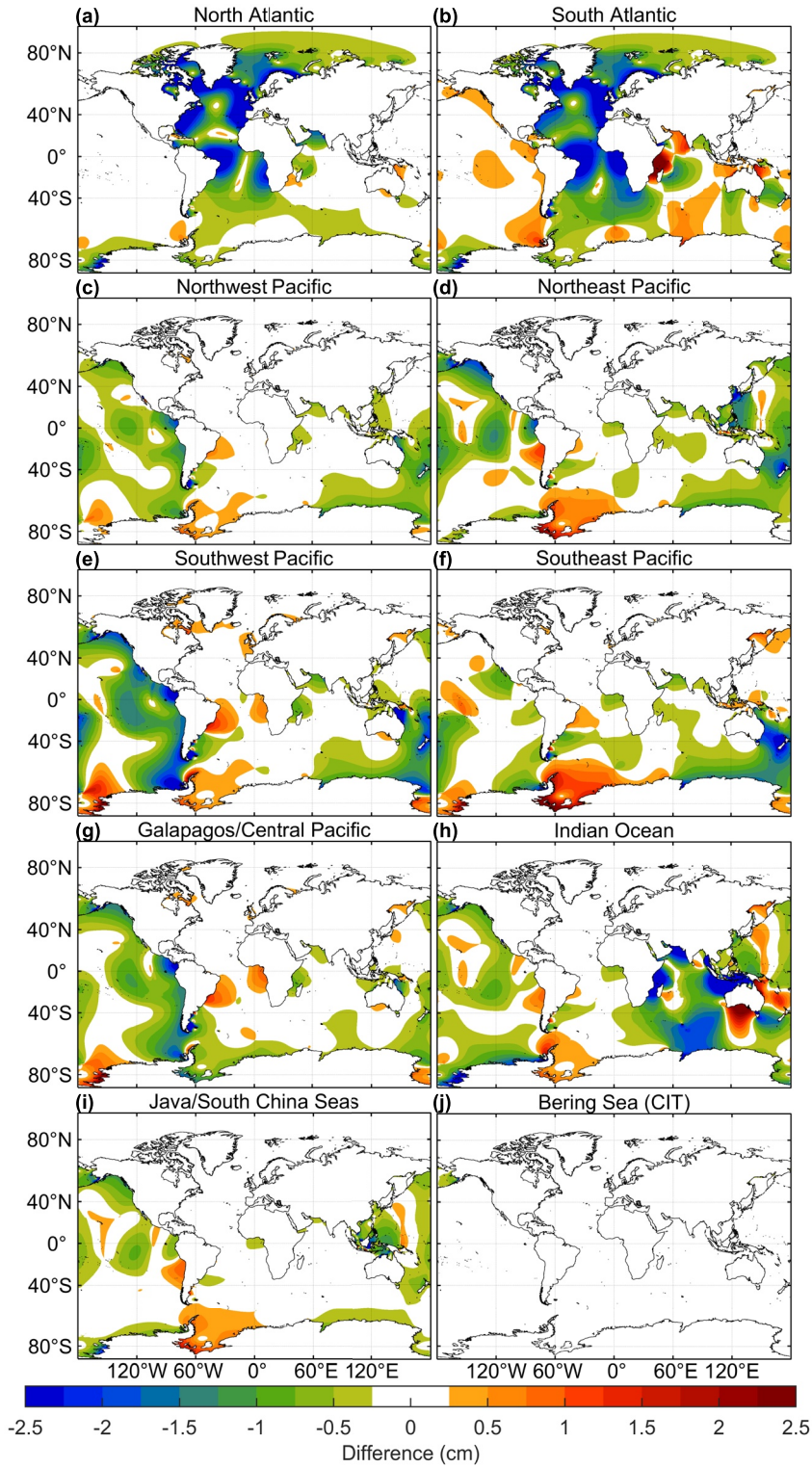

Figure 11. Responses in M_2 amplitude to perturbing C_{ii} by 0.2 within certain regions. Note that most show heavily nonlocal effects. Also note the overlap in responses especially between regions in the same oceans. Japan/Ohkotsk Seas and East China/Yellow Seas regions were omitted because they showed only local effects.

for Manning's n. In these local re-optimizations, regions such as the European Shelf were subdivided into smaller regions (Irish Sea, English Channel, and European Shelf), individually perturbed once more, and the cost function minimization was reapplied only within the European shelf. While these local re-optimizations somewhat degraded deep ocean results globally, the shallow water solutions improved drastically, especially in the regions in which this treatment was used (Figures 12g and 12h). Tables 2 and 3 summarize the optimized coefficients.

6.2.1. Manning's n

We find that the values derived in our optimization process are consistent with the physical and geometric properties of the various regions and flows. By correlating Table 2 with Figure 3a, we note that most of the high energy areas tend toward a Manning's n around 0.028 $s\,m^{-1/3}$. Such areas include Baffin Bay (0.027 $s\,m^{-1/3}$), the Bass Strait (0.025 $s\,m^{-1/3}$), the English Channel (0.026 $s\,m^{-1/3}$), the European Shelf (0.026 $s\,m^{-1/3}$), Georges Bank (0.033 $s\,m^{-1/3}$), the Gulf of Maine (0.035 $s\,m^{-1/3}$), and Hudson Bay (0.029 $s\,m^{-1/3}$). All of these regions were identified as having high dissipation rates. The reason for these consistent values of Manning's n is the high velocity currents tend to strip away fine sediments leaving a rougher higher friction surface and/or create large ripples and dunes on the seabed, resulting in higher Manning's n than the typical 0.022 $s\,m^{-1/3}$ value.

An important qualifier to this trend is the case of the Aleutian and Ryuku Islands. When setting the upper limit to 0.050 $s\,m^{-1/3}$ for optimized Manning values, there was still a large over prediction throughout the Bering Sea and Shelf as well as within the Korean Strait and Yellow Sea. High velocity flows and the presence of eddying increase turbulence, increasing the boundary layer dissipation, which can be approximated by using a higher Manning's n. In order to capture some of this dissipation without sacrificing accuracy in other regions, the Aleutian and Ryuku islands were separated from their respective regions (Bering and East China Seas, respectively) and the upper limit on Manning's n was removed. The new optimized value for Manning became 0.087 $s\,m^{-1/3}$ for the Aleutians, which is high, but still physically reasonable, and was capped at 0.099 $s\,m^{-1/3}$ for the Ryuku Islands lest it degrades results. Additionally, several regions, which past studies have shown to require low friction, such as the Yellow Sea, require lower than the widely used value of 0.022 $s\,m^{-1/3}$ (Pringle et al., 2018). While the Yellow Sea does dissipate a large amount of tidal energy (see Figure 3a), this marginal sea is characterized by fine sediments. These sediments result in a lower than usual Manning's n. Another interesting note is the optimal value for the Arctic Ocean and Northwest Passage. These regions have Manning values of 0.042 and 0.048 $s\,m^{-1/3}$, respectively, higher than most of the highly dissipative regions. This higher friction is due to the presence of sea ice in those regions, which creates two interfaces of boundary layer friction—the bottom of the ocean and the bottom of the ice cover, effectively doubling friction as the optimization suggests.

In addition to the global optimization performed here, we showed through the local re-optimizations of the European Shelf, the Yellow/East China/Japan Seas, and the Puget Sound/Strait of Georgia that this methodology could be used to locally improve friction parameters in regions of interest.

6.2.2. Coefficient of Internal Tides

Table 3 shows the optimized internal tide parameters found for our defined regions. In terms of major ocean basins, the northern Pacific and Galapagos have low values (1.0–1.4), the Atlantic and Indian Ocean have intermediate values (1.7–2.4), and the southern Pacific has high values (3.4–3.8). The Galapagos region, ringed by muted underwater mountain chains was defined to alleviate consistent under-predictions in that region. We examined if there was a relationship between mean topographic gradients and the optimal C_{it} values but were unable to find a correlation.

Marginal seas with deep ocean island chains lead to high values of the internal tide coefficient. The Bering Sea, the Java Sea, and the Yellow Sea all result in very high C_{it} values (all capping out at 4.0). The optimization is likely capturing some of the flows crossing these steep underwater mountain chains generating internal waves but may also be adding damping to capture the unresolved vertical and horizontal eddy structures.

There are several reasons that the C_{it} does not optimize as neatly as boundary layer dissipation. First, the parameterization of internal tide conversion is still somewhat mesh and resolution-dependent. While computing topographic gradients directly from the GEBCO (2020) database and placing higher resolution on shelf breaks and ridges to better define cross ridge currents mitigates the issue, it cannot eliminate the dependency since the topographic gradients are still mesh size averaged. In addition, there are exterior factors that affect the optimal C_{it} values. Foremost among these is the complexity of the barotropic to baroclinic conversion phenomenon.

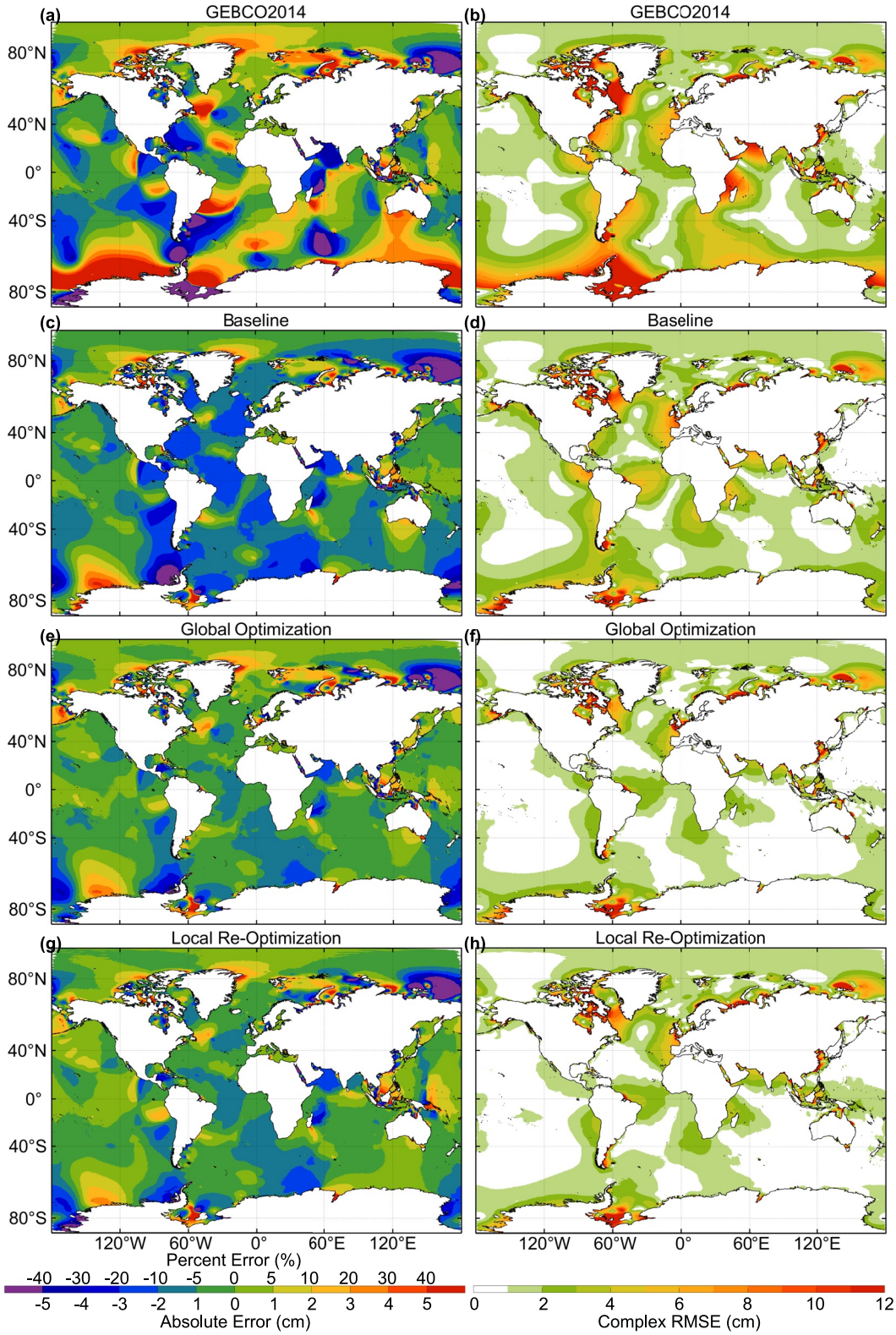

Figure 12. Progression of error from GEBCO (2014) with base friction values to Global Baseline, to Global Optimization, and to Local Re-Optimization. Figures on left show amplitude error compared to TPXO9 based on error brackets as seen in the colorbar with the minimum bracket of either percentage or absolute error being displayed. This allows for accurate representations of error to be displayed. For instance, at amphidromic points, a small absolute error produces a large percentage error and hence the solution appears worse than it is. Figures on right show the complex error (in this case mean discrepancy from TPXO9).

Table 3
Optimized C_{it} Values

Region	Optimal C_{it}
North Atlantic	1.7
South Atlantic	2.4
Bering Sea	4.0
NE Pacific	1.4
SE Pacific	3.8
NW Pacific	1.2
SW Pacific	3.4
Galapagos	1.0
Indian Ocean	2.2
Japan Sea	1.0
Java Sea	4.0
Yellow Sea	4.0

While internal tide dissipation has been studied for decades (Garrett & Kunze, 2007), there is uncertainty in the best method to model and parameterize this complicated process. Additionally, the use of decadally averaged salinity and temperature fields from observational data could result in imperfect depth-averaged values, missing both resolution and seasonal variability. Finally, we are missing ocean current systems in the computations. Despite these challenges, there can be no doubt that this optimization scheme greatly improved tidal results in this model both in the deep ocean and in coastal areas.

7. Summary and Discussion

Our exploration of global tides with a high resolution mesh targeted to the nearshore and high topographic length scales has led to a high fidelity solution without applying data assimilation. We found that tides are highly sensitive to bathymetry in select regions. The Ronne Ice Shelf definition appears to control Atlantic tides by controlling resonance. On the other hand the Foxe Basin bathymetry, north of Hudson Bay, controls Atlantic tides by controlling dissipation. By exploring boundary layer and internal tide dissipation, we have been able to pinpoint where dissipation is concentrated. Boundary layer dissipation in particular is highly focused with only 1.4% of the ocean dissipating 90% and 4.3% of the ocean dissipating 99%. The most concentrated dissipation regions include the Foxe Basin, Georges Bank, the English Channel, Strait of Dover, and the Patagonian Shelf and Northeast Brazilian Shelf. The Manning n coefficients derived through the optimization process align well with the regional physical characterizations of high energy dissipation zones, ice covered regions and deep ocean island chains. Internal tide dissipation is much more diffusely distributed compared to bottom boundary layer dissipation, by an order of magnitude.

The simplest method to evaluate the results of the optimization is to examine the global error metrics as seen in Table 4. First, let us consider the comparisons to TPXO9. In the overall mean discrepancy from TPXO, there is an improvement from the global baseline to the local re-optimization of almost 0.6 cm in the M_2 constituent. In the deep ocean, the global optimization improves the results by over a centimeter. Unfortunately this improvement is to the detriment of the shallow solution. Re-optimizing improves the shallow solution compared to TPXO by 0.36 cm for the M_2 over the global optimization (a net improvement from the global baseline of 0.2 cm). At the same time, the deep water solution degrades slightly; however, it is still a net improvement of 0.86 cm.

Deep and shallow station results improve in the same pattern as when comparing to TPXO9. Coastal stations, on the other hand, have a different trend and improve over both steps of the optimization. With a net improvement of 1.11 cm, the shallow station error metric is where the most global improvement is seen.

For constituents other than the M_2, there is, generally, improvement for semidiurnal constituents. Despite not being included in the cost function, the S_2, N_2, and K_2 all show improvement in most error metrics (the exceptions being the mean discrepancy compared to stations in shallow regions for the S_2 and K_2). It should be noted that this model does not include atmospheric pressure forcing, which is important in accurately modeling the S_2 tide. The diurnal constituents, on the other hand largely stayed the same or degraded slightly overall. While select error metrics for the diurnal constituents did show modest improvement, there is not an obvious trend. Importantly, the 8 constituent error metrics all improved.

Figure 12 also highlights the improvements in spatial distribution of differences to TPXO9 and shows that in certain basins they are far better than the global error metric indicators. The under-prediction throughout the Atlantic Ocean is largely solved and much of the Pacific Ocean has also improved. Figure 12a through Figure 12d are included to again highlight the magnitude of improvement that can be seen by using higher quality bathymetry over and above any improvement that could hope to be seen by tuning friction factors. Simply by upgrading the bathymetry, especially in the Antarctic ice shelves and in Hudson Bay, the entirety of the globe shows dramatic improvement.

Table 4
Summary of Mean Discrepancy for Major Eight Constituents for Baseline, Globally Optimized, and Locally Re-Optimized Runs

Const.	Error metric	Global baseline	Global optimization	Local re-optimization
8 Const	$\bar{D}_{tpxo,overall}$	5.18	4.61	4.59
	$\bar{D}_{tpxo,deep}$	3.94	3.03	3.11
	$\bar{D}_{tpxo,shallow}$	11.15	11.18	10.90
	$\bar{D}_{sta,deep}$	3.75	3.04	3.18
	$\bar{D}_{sta,shallow}$	10.18	13.74	9.77
	$\bar{D}_{sta,coast}$	9.67	9.26	8.85
M_2	$\bar{D}_{tpxo,overall}$	3.70	3.10	3.10
	$\bar{D}_{tpxo,deep}$	2.81	1.77	1.94
	$\bar{D}_{tpxo,shallow}$	7.96	8.10	7.74
	$\bar{D}_{sta,deep}$	2.67	1.72	1.94
	$\bar{D}_{sta,shallow}$	7.18	9.52	6.16
	$\bar{D}_{sta,coast}$	6.47	6.02	5.63
S_2	$\bar{D}_{tpxo,overall}$	2.83	2.49	2.45
	$\bar{D}_{tpxo,deep}$	2.37	2.09	2.03
	$\bar{D}_{tpxo,shallow}$	5.34	4.72	4.71
	$\bar{D}_{sta,deep}$	2.41	2.19	2.19
	$\bar{D}_{sta,shallow}$	4.93	6.12	5.12
	$\bar{D}_{sta,coast}$	4.27	4.09	4.17
N_2	$\bar{D}_{tpxo,overall}$	0.77	0.70	0.72
	$\bar{D}_{tpxo,deep}$	0.56	0.39	0.43
	$\bar{D}_{tpxo,shallow}$	1.75	1.83	1.85
	$\bar{D}_{sta,deep}$	0.51	0.38	0.43
	$\bar{D}_{sta,shallow}$	1.76	2.02	1.64
	$\bar{D}_{sta,coast}$	1.40	1.33	1.32
K_2	$\bar{D}_{tpxo,overall}$	0.90	0.47	0.48
	$\bar{D}_{tpxo,deep}$	0.59	0.32	0.32
	$\bar{D}_{tpxo,shallow}$	2.20	1.13	1.14
	$\bar{D}_{sta,deep}$	0.41	0.36	0.36
	$\bar{D}_{sta,shallow}$	1.01	1.37	1.03
	$\bar{D}_{sta,coast}$	1.14	1.09	1.04
K_1	$\bar{D}_{tpxo,overall}$	1.67	1.83	1.83
	$\bar{D}_{tpxo,deep}$	1.01	1.05	1.06
	$\bar{D}_{tpxo,shallow}$	4.26	4.78	4.76
	$\bar{D}_{sta,deep}$	0.54	0.73	0.74
	$\bar{D}_{sta,shallow}$	1.84	1.99	1.80
	$\bar{D}_{sta,coast}$	1.71	1.87	2.00

Table 4
Continued

Const.	Error metric	Global baseline	Global optimization	Local re-optimization
O_1	$\bar{D}_{tpxo,overall}$	0.78	1.00	1.00
	$\bar{D}_{tpxo,deep}$	0.44	0.51	0.54
	$\bar{D}_{tpxo,shallow}$	2.06	2.73	2.67
	$\bar{D}_{sta,deep}$	0.28	0.34	0.38
	$\bar{D}_{sta,shallow}$	1.00	1.35	1.04
	$\bar{D}_{sta,coast}$	1.10	1.17	1.29
P_1	$\bar{D}_{tpxo,overall}$	0.53	0.51	0.52
	$\bar{D}_{tpxo,deep}$	0.32	0.23	0.28
	$\bar{D}_{tpxo,shallow}$	1.34	1.36	1.38
	$\bar{D}_{sta,deep}$	0.18	0.19	0.20
	$\bar{D}_{sta,shallow}$	0.65	0.66	0.67
	$\bar{D}_{sta,coast}$	0.64	0.68	0.70
Q_1	$\bar{D}_{tpxo,overall}$	0.18	0.21	0.21
	$\bar{D}_{tpxo,deep}$	0.12	0.12	0.13
	$\bar{D}_{tpxo,shallow}$	0.44	0.53	0.54
	$\bar{D}_{sta,deep}$	0.18	0.18	0.17
	$\bar{D}_{sta,shallow}$	0.71	0.68	0.67
	$\bar{D}_{sta,coast}$	0.33	0.33	0.35

Note. All error metrics are given in centimeters.

The improvement from the global optimization (Figures 12e and 12f) to the local re-optimization (Figures 12g and 12h) is more subtle. By performing the re-optimization, results on the European Shelf were significantly improved. Other regions this procedure was used were in the Yellow and East China Seas. These two regions were further divided into the Sea of Japan, Korean Strait, Yellow Sea, and South China Sea. Again, this procedure greatly improved local solutions. Remaining errors are largely found in high latitude ice-covered regions and nearshore high energy regions.

Boundary layer dissipation for our re-optimized model accounted for 1.83 TW of boundary layer dissipation and 1.49 TW of internal tide dissipation. This brings the total dissipation to 3.31 TW, less than the widely accepted 3.5 TW. Note that we did not include lateral viscous dissipation, which likely plays a role in the high energy dissipation regions. Previous investigators attributed 0.9, 1.0, and 1.18 TW (Egbert & Ray, 2000; Green & Nycander, 2013; Munk & Wunsch, 1998) to internal tide dissipation and as such, our estimates continue the trend of an increasingly larger proportion of the total being attributed to internal tide dissipation. Our larger number is a result of both attribution; we compute energy dissipation directly at computational nodes as well as our focusing resolution on steep topographic gradients. When we do not resolve steep topographic gradients, our dissipation estimates fall in line with previously published estimates.

Overall our optimized solution has very low error metrics when compared to both TPXO9 as well as tidal station data. Certainly bathymetry in a few select locations plays a large role in tidal fidelity. Internal tide generation is vital to obtain accurate results in the deep ocean, and boundary layer dissipation is also critical in high energy regions of limited extent. Our findings show that small changes in the amounts of boundary layer and internal tide dissipation can have wide reaching effects on global tides. Understanding regions that are particularly sensitive to alterations in seabed roughness, ocean stratification, and other factors that control dissipation is vital to developing accurate tidal models for a changing climate. Furthermore, as we have demonstrated, it is possible to use this knowledge to efficiently find frictional parameters that are consistent with the energetics of the very limited high dissipation regions.

Global and local fidelity can be improved through improved regional mesh refinement and bathymetry, particularly in the hot spot regions that we have identified. More broadly, inner shelf improvements in mesh resolution and bathymetry will always improve nearshore tides (Pringle et al., 2018). For example, we are entirely missing the Wadden Sea in our model, a more than 500 km stretch of tidal flats along the eastern North Sea with a 1–4 m tidal range leading to significant regional dissipation. Furthermore, improvements can be achieved by refining the underlying physics in our model. We certainly oversimplified the treatment of the Ronne Ice Shelf by defining bathymetry equal to the water column height between the ocean floor and the bottom of the ice shelf. The physics is much more complex with three dimensional circulation with spatially varying density fields and a flexible ice shelf. Finally, using modeled high resolution baroclinic information would not only improve the resolution of our vertical density gradient information used in the internal tide dissipation model, it would also allow us to capture the seasonality of internal tide dissipation, which is known to vary throughout the year due to changing density and buoyancy. In addition, incorporating time varying salinity and temperature profiles from a global ocean model would allow us to efficiently drive baroclinic pressure gradient terms driving major ocean current systems such as the Gulf Stream and Kuroshio Current (Metzger et al., 2017; Pringle et al., 2019).

Data Availability Statement

Version 3.3 of OceanMesh2D can be found at doi: https://doi.org/10.5281/zenodo.4386220. Selected results from perturbation runs, the list of tidal stations used with amplitudes and phases calculated, and results from the Baseline, Global Optimization, and Local Re-Optimization can be found at doi: https://doi.org/10.5281/zenodo.5563024. ADCIRC v55 is available by request at www.adcirc.org.

Acknowledgments
This study was funded by the National Oceanic and Atmospheric Administration through FY18 JTTI grant NA18OAR4590377 and the National Science Foundation NCER PREEVENTS Track 2 grant ICER-1855047. William J. Pringle was supported by NOAA through the University Corporation for Atmospheric Research Grant No. NA19OAR0220123. Joannes J. Westerink was supported in part by the Joseph and Nona Ahearn endowment at the University of Notre Dame. Joannes J. Westerink and Damrongsak Wirasaet were supported in part by Department of Energy Grant No. DOE DE-SC0021105.

References

Arbic, B. K., Alford, M. H., Ansong, J. K., Buijsman, M. C., Ciotti, R. B., Farrar, J. T., et al. (2018). A primer on global internal tide and internal gravity wave continuum modeling in HYCOM and MITGCM. *New Frontiers in Operational Oceanography*. https://doi.org/10.17125/gov2018.ch13

Arbic, B. K., Karsten, R. H., & Garrett, C. (2009). On tidal resonance in the global ocean and the back-effect of coastal tides upon open-ocean tides. *Atmosphere-Ocean*, *47*(4), 239–266. https://doi.org/10.3137/OC311.2009

Arcement, G. J., & Schneider, V. R. (1989). *Guide for selecting Manning's roughness coefficients for natural channels and flood plains*(- ed.; Tech. Rep.). https://doi.org/10.3133/wsp2339

Atkinson, J. H., Roberts, H., Hagen, S., Zou, S., Bacopoulos, P., Medeiros, S., et al. (2011). Deriving frictional parameters and performing historical validation for an ADCIRC storm surge model of the Florida Gulf coast. *Florida Watershed Journal*, *4*.

Atkinson, J. H., Westerink, J. J., & Hervouet, J. M. (2004). Similarities between the quasi-bubble and the generalized wave continuity equation solutions to the shallow water equations. *International Journal for Numerical Methods in Fluids*, *45*(7), 689–714. https://doi.org/10.1002/fld.700

Atkinson, J. H., Westerink, J. J., & Luettich, R. A., Jr. (2004). Two-dimensional dispersion analyses of finite element approximations to the shallow water equations. *International Journal for Numerical Methods in Fluids*, *45*(7), 715–749. https://doi.org/10.1002/fld.701

Beaman, R. (2018). *High-resolution depth model for the northern Australia—100 m* [Data set].

Blakely, C. (2021). *Data supporting dissipation and bathymetric sensitivities in an unstructured mesh global tidal model* [Data set]. https://doi.org/10.5281/zenodo.5563024

Boyer, T. P., Antonov, J. I., Baranova, O. K., Garcia, H. E., Johnson, D. R., Mishonov, A. V., et al. (2013). *World ocean database 2013*. https://doi.org/10.7289/V5NZ85MT

Bunya, S., Dietrich, J. C., Westerink, J. J., Ebersole, B. A., Smith, J. M., Atkinson, J. H., et al. (2010). A high-resolution coupled riverine flow, tide, wind, wind wave, and storm surge model for southern Louisiana and Mississippi. Part I: Model development and validation. *Monthly Weather Review*, *138*(2), 345–377. https://doi.org/10.1175/2009MWR2906.1

Chow, V. T. (1959). *Open-channel hydraulics*. McGraw-Hill.

CHS. (2018). *Canadian hydrographic service non-navigational (NONNA) bathymetric data* [Data set]. Retrieved from https://open.canada.ca/data/en/dataset/d3881c4c-650d-4070-bf9b-1e00aabf0a1d

Dresback, K. M., Kolar, R. L., & Luettich, R. A., Jr. (2006). On the form of the momentum equation and lateral stress closure law in shallow water modeling. In *Estuarine and coastal modeling* (pp. 399–418).

Egbert, G. D., & Erofeeva, S. Y. (2002). Efficient inverse modeling of barotropic ocean tides. *Journal of Atmospheric and Oceanic Technology*, *19*(2), 183–204. https://doi.org/10.1175/1520-0426(2002)019<0183:EIMOBO>2.0.CO;2

Egbert, G. D., & Erofeeva, S. Y. (2021). *TPXO9-Atlas* [Data set]. Retrieved from https://www.tpxo.net/global/tpxo9-atlas

Egbert, G. D., & Ray, R. D. (2000). Significant dissipation of tidal energy in the deep ocean inferred from satellite altimeter data. *Nature*, *405*(6788), 775–778. https://doi.org/10.1038/35015531

Egbert, G. D., & Ray, R. D. (2001). Estimates of M2 tidal energy dissipation from TOPEX/Poseidon altimeter data. *Journal of Geophysical Research*, *106*(C10), 22475–22502. https://doi.org/10.1029/2000JC000699

Garrett, C., & Kunze, E. (2007). Internal tide generation in the deep ocean. *Annual Review of Fluid Mechanics*, *39*(1), 57–87. https://doi.org/10.1146/annurev.fluid.39.050905.110227

GEBCO, B. C. G. (2014). *The GEBCO_2014 grid, version 20150318* [Data set]. Retrieved from https://www.bodc.ac.uk/data/open_download/gebco/GEBCO_30SEC/zip/

GEBCO, B. C. G. (2019). *The GEBCO_2019 Grid—A continuous terrain model of the global oceans and land* [Data set]. https://doi.org/10.5285/836f016a-33be-6ddc-e053-6c86abc0788e

GEBCO, B. C. G. (2020). *The GEBCO_2020 Grid - a continuous terrain model of the global oceans and land* [Data set]. https://doi.org/10.5285/a29c5465-b138-234d-e053-6c86abc040b9

Graham, L., Butler, T., Walsh, S., Dawson, C., & Westerink, J. J. (2017). A measure-theoretic algorithm for estimating bottom friction in a coastal inlet: Case study of bay St. Louis during hurricane Gustav (2008). *Monthly Weather Review*, *145*(3), 929–954. https://doi.org/10.1175/MWR-D-16-0149.1

Green, J. A. M., & Nycander, J. (2013). A comparison of tidal conversion parameterizations for tidal models. *Journal of Physical Oceanography*, *43*(1), 104–119. https://doi.org/10.1175/JPO-D-12-023.1

Haigh, I. D., Pickering, M. D., Green, J. A. M., Arbic, B. K., Arns, A., Dangendorf, S., et al. (2020). The tides they are a-changin': A comprehensive review of past and future nonastronomical changes in tides, their driving mechanisms, and future implications. *Reviews of Geophysics*, *58*(1), e2018RG000636. https://doi.org/10.1029/2018RG000636

Harris, P. T., Macmillan-Lawler, M., Rupp, J., & Baker, E. K. (2014). Geomorphology of the oceans. *Marine Geology*, *352*, 4–24. https://doi.org/10.1016/j.margeo.2014.01.011

Hope, M., Westerink, J. J., Kennedy, A. B., Kerr, P., Dietrich, J., Dawson, C., et al. (2013). Hindcast and validation of Hurricane Ike (2008) waves, forerunner, and storm surge. *Journal of Geophysical Research*, *118*(9), 4424–4460. https://doi.org/10.1002/jgrc.20314

Jeffreys, H. (1921). Tidal friction in shallow seas. *Philosophical Transactions of the Royal Society of London - Series A: Containing Papers of a Mathematical or Physical Character*, *221*, 239–264.

Jeon, C.-H., Buijsman, M. C., Wallcraft, A. J., Shriver, J. F., Arbic, B. K., Richman, J. G., & Hogan, P. J. (2019). Improving surface tidal accuracy through two-way nesting in a global ocean model. *Ocean Modelling*, *137*, 98–113. Retrieved from https://www.sciencedirect.com/science/article/pii/S1463500318301665

Kennedy, A. B., Gravois, U., Zachry, B. C., Westerink, J. J., Hope, M. E., Dietrich, J. C., et al. (2011). Origin of the hurricane Ike forerunner surge. *Geophysical Research Letters*, *38*(8). https://doi.org/10.1029/2011GL047090

Kerr, P. C., Martyr, R. C., Donahue, A. S., Hope, M. E., Westerink, J. J., Luettich, R. A., Jr., et al. (2013). U.S. IOOS coastal and ocean modeling testbed: Evaluation of tide, wave, and hurricane surge response sensitivities to mesh resolution and friction in the Gulf of Mexico. *Journal of Geophysical Research: Oceans*, *118*(9), 4633–4661. https://doi.org/10.1002/jgrc.20305

Lefèvre, F., Le Provost, C., & Lyard, F. H. (2000). How can we improve a global ocean tide model at a regional scale? A test on the Yellow Sea and the East China Sea. *Journal of Geophysical Research*, *105*(C4), 8707–8725. https://doi.org/10.1029/1999JC900281

Luettich, R., & Westerink, J. (2004). *Formulation and numerical implementation of the 2D/3D ADCIRC finite element model version 44.XX (Tech. Rep.)*. Retrieved from https://adcirc.org/wp-content/uploads/sites/2255/2018/11/adcirc_theory_2004_12_08.pdf

Lyard, F., Allain, D. J., Cancet, M., Carrère, L., & Picot, N. (2021). Fes2014 global ocean tide atlas: Design and performance. *Ocean Science*, *17*(3), 615–649. https://doi.org/10.5194/os-17-615-2021

Lyard, F., Lefevre, F., Letellier, T., & Francis, O. (2006). Modelling the global ocean tides: Modern insights from FES2004. *Ocean Dynamics*, *56*(5), 394–415. https://doi.org/10.1007/s10236-006-0086-x

MATLAB. (2018). *9.7.0.1190202 (r2019b)*. The MathWorks Inc.

Metzger, J. E., Helber, R. W., Hogan, P. J., Poset, P. G., Thoppil, P. G., Townsend, T. L., & Wallcraft, A. J. (2017). *Global ocean forecast system 3.1 validation testing (Tech. Rep.)*. Naval Research Laboratory.

Munk, W. (1997). Once again: Once again—Tidal friction. *Progress in Oceanography*, *40*(1), 7–35. https://doi.org/10.1016/S0079-6611(97)00021-9

Munk, W., & Wunsch, C. (1998). Abyssal recipes II: Energetics of tidal and wind mixing. *Deep Sea Research Part I: Oceanographic Research Papers*, *45*(12), 1977–2010. Retrieved from https://www.sciencedirect.com/science/article/pii/S0967063798000703

Pringle, W. J. (2017). *Global tide gauge database* [Data set]. Retrieved from https://www.google.com/maps/d/u/0/viewer?mid=1yvnYoLUFS9kcB5LnJEdyxk2qz6g&ll=-3.81666561775622e-14\%2C101.96502786483464&z=2

Pringle, W. J., Gonzalez-Lopez, J., Joyce, B. R., Westerink, J. J., & van der Westhuysen, A. J. (2019). Baroclinic coupling improves depth-integrated modeling of coastal sea level variations around Puerto Rico and the U.S. Virgin Islands. *Journal of Geophysical Research: Oceans*, *124*(3), 2196–2217. https://doi.org/10.1029/2018JC014682

Pringle, W. J., Wirasaet, D., Roberts, K. J., & Westerink, J. J. (2021). Global storm tide modeling with ADCIRC v55: Unstructured mesh design and performance. *Geoscientific Model Development*, *14*(2), 1125–1145. https://doi.org/10.5194/gmd-14-1125-2021

Pringle, W. J., Wirasaet, D., Suhardjo, A., Meixner, J., Westerink, J. J., Kennedy, A. B., & Nong, S. (2018). Finite-Element barotropic model for the Indian and Western Pacific Oceans: Tidal model-data comparisons and sensitivities. *Ocean Modelling*, *129*, 13–38. https://doi.org/10.1016/j.ocemod.2018.07.003

Qian, S., Wang, D., Zhang, J., & Li, C. (2021). Adjoint estimation and interpretation of spatially varying bottom friction coefficients of the M2 tide for a tidal model in the Bohai, yellow and east China seas with multi-mission satellite observations. *Ocean Modelling*, *161*, 101783. Retrieved from https://www.sciencedirect.com/science/article/pii/S1463500321000330

Roberts, K. J., & Pringle, W. J. (2018). *Oceanmesh2d: User guide—Precise distance-based two-dimensional automated mesh generation toolbox intended for coastal ocean/shallow water*(Tech. Rep.). https://doi.org/10.13140/RG.2.2.21840.61446/2

Roberts, K. J., Pringle, W. J., & Westerink, J. J. (2019). OceanMesh2D 1.0: MATLAB-based software for two-dimensional unstructured mesh generation in coastal ocean modeling. *Geoscientific Model Development*, *12*(5), 1847–1868. https://doi.org/10.5194/gmd-12-1847-2019

Schaffer, J., Timmermann, R., Arndt, J. E., Rosier, S. H. R., Anker, P. G. D., Roberts, D. H., et al. (2019). An update to Greenland and Antarctic ice sheet topography, cavity geometry, and global bathymetry (RTopo-2.0.4). PANGAEA. (Supplement to: Schaffer, Janin; Kanzow, Torsten; von Appen, Wilken-Jon; von Albedyll, Luisa; Arndt, Jan Erik; Roberts, David H (2020): Bathymetry constrains ocean heat supply to Greenland's largest glacier tongue. *Nature Geoscience*, *13*(3), 227–231. https://doi.org/10.1594/PANGAEA.905295

Smagorinsky, J. (1963). General circulation experiments with the primitive equations: I. The basic experiment. *Monthly Weather Review*, *91*(3), 99–164. https://doi.org/10.1175/1520-0493(1963)091<0099:GCEWTP>2.3.CO;2

Stammer, D., Ray, R. D., Andersen, O. B., Arbic, B. K., Bosch, W., Carrère, L., et al. (2014). Accuracy assessment of global barotropic ocean tide models. *Reviews of Geophysics*, *52*(3), 243–282. https://doi.org/10.1002/2014RG000450

Sulzbach, R., Dobslaw, H., & Thomas, M. (2021). High-resolution numerical modeling of barotropic global ocean tides for satellite gravimetry. *Journal of Geophysical Research: Oceans*, *126*(5), e2020JC017097. https://doi.org/10.1029/2020JC017097

Taylor, G. I., & Shaw, W. N. (1920). I. Tidal friction in the Irish Sea. *Philosophical Transactions of the Royal Society of London - Series A: Containing Papers of a Mathematical or Physical Character*, *220*(571–581), 1–33. https://doi.org/10.1098/rsta.1920.0001

Wang, D., Zhang, J., & Wang, Y. P. (2021). Estimation of bottom friction coefficient in multi-constituent tidal models using the adjoint method: Temporal variations and spatial distributions. *Journal of Geophysical Research: Oceans*, *126*(5), e2020JC016949. https://doi.org/10.1029/2020JC016949

Wang, X., Chao, Y., Shum, C., Yi, Y., & Fok, H. S. (2012). Comparison of two methods to assess ocean tide models. *Journal of Atmospheric and Oceanic Technology*, *29*(8), 1159–1167. https://doi.org/10.1175/JTECH-D-11-00166.1

Wang, X., Verlaan, M., Apecechea, M. I., & Lin, H. X. (2021). Computation-efficient parameter estimation for a high-resolution global tide and surge model. *Journal of Geophysical Research: Oceans*, *126*(3). https://doi.org/10.1029/2020JC016917

Westerink, J., Luettich, R., Feyen, J. C., Atkinson, J. H., Dawson, C., Roberts, H. J., et al. (2008). A basin- to channel-scale unstructured grid hurricane storm surge model applied to southern Louisiana. *Monthly Weather Review*, *136*(3), 833–864. https://doi.org/10.1175/2007mwr1946.1

Westerink, J., Luettich, R., Jr., Blain, C., & Scheffner, N. (1994). *Adcirc: An advanced three-dimensional circulation model for shelves, coasts, and estuaries. Report 2. User's manual for adcirc-2ddi*(Tech. Rep.).

Wilmes, S.-B., & Green, J. A. M. (2014). The evolution of tides and tidal dissipation over the past 21,000 years. *Journal of Geophysical Research: Oceans*, *119*(7), 4083–4100. https://doi.org/10.1002/2013JC009605

Zaron, E. D., & Egbert, G. D. (2006). Estimating open-ocean barotropic tidal dissipation: The Hawaiian ridge. *Journal of Physical Oceanography*, *36*(6), 1019–1035. https://doi.org/10.1175/JPO2878.1